The Astrophysical Journal, 892:102 (20pp), 2020 April 1 https://doi.org/10.3847/1538-4357/ab7997

X-Ray Scaling Relations for a Representative Sample of Planck-selected Clusters Observed with *XMM-Newton*

Lorenzo Lovisari[1], Gerrit Schellenberger[1], Mauro Sereno[2,3], Stefano Ettori[2,3], Gabriel W. Pratt[4], William R. Forman[1], Christine Jones[1], Felipe Andrade-Santos[1], Scott Randall[1], and Ralph Kraft[1]
[1] Center for Astrophysics|Harvard & Smithsonian, 60 Garden Street, Cambridge, MA 02138, USA; lorenzo.lovisari@cfa.harvard.edu
[2] INAF—Osservatorio di Astrofisica e Scienza dello Spazio di Bologna, via Piero Gobetti 93/3, I-40129 Bologna, Italia
[3] INFN, Sezione di Bologna, viale Berti Pichat 6/2, I-40127 Bologna, Italy
[4] AIM, CEA, CNRS, Université Paris-Saclay, Université Paris Diderot, Sorbonne Paris Cité, F-91191 Gif-sur-Yvette, France
Received 2019 November 25; revised 2020 February 7; accepted 2020 February 23; published 2020 April 2

Abstract

We report the scaling relations derived by fitting the X-ray parameters determined from analyzing the *XMM-Newton* observations of 120 galaxy clusters in the Planck Early Sunyaev–Zel'dovich (SZ) sample spanning the redshift range of $0.059 < z < 0.546$. We find that the slopes of all the investigated scaling relations significantly deviate from the self-similar predictions, if self-similar redshift evolution is assumed. When the redshift evolution is left free to vary, the derived slopes are more in agreement with the self-similar predictions. Relaxed clusters have on average ∼30% higher X-ray luminosity than disturbed clusters at a given mass, a difference that, depending on the relative fraction of relaxed and disturbed clusters in the samples (e.g., SZ vs. X-ray selected), has a strong impact on the normalization obtained in different studies. Using the core-excised cluster luminosities reduces the scatter and brings into better agreement the L–$M_{\rm tot}$ and L–T relations determined for different samples. $M_{\rm tot}$–T, $M_{\rm tot}$–$Y_{\rm X}$, and $M_{\rm tot}$–$M_{\rm gas}$ relations show little dependence on the dynamical state of the clusters, but the normalizations of these relations may depend on the mass range investigated. Although most of the clusters investigated in this work reside at relatively low redshift, the fits prefer values of γ, the parameter accounting for the redshift evolution, different from the self-similar predictions. This suggests an evolution ($<2\sigma$ level, with the exception of the $M_{\rm tot}$–T relation) of the scaling relations. For the first time, we find significant evolution ($>3\sigma$) of the $M_{\rm tot}$–T relation, pointing to an increase of the kinetic-to-thermal energy ratio with redshift. This is consistent with a scenario in which higher-redshift clusters are on average more disturbed than their lower-redshift counterparts.

Unified Astronomy Thesaurus concepts: Galaxy clusters (584); Intracluster medium (858); Observational cosmology (1146); X-ray astronomy (1810)

Supporting material: machine-readable table

1. Introduction

X-ray and Sunyaev–Zel'dovich (SZ) surveys are two independent probes of the same physical component in galaxy clusters: the hot gas filling the space between galaxies. However, these surveys have a different dependence on the gas density: the X-ray emission scales with the square of the electron gas density, while the SZ effect scales linearly. Due to that, the SZ experiments detect a larger fraction of disturbed systems than the X-ray surveys, which detect more centrally peaked and relaxed galaxy clusters (Rossetti et al. 2016, 2017; Andrade-Santos et al. 2017; Lovisari et al. 2017; Bartalucci et al. 2019). This is an important fact because relaxed and disturbed clusters populate a different region of the residual space with respect to the best-fit L–$M_{\rm tot}$ and L–T relations, with relaxed (disturbed) objects having, on average, an X-ray luminosity higher (lower) than the mean (e.g., Pratt et al. 2009; see, e.g., Figures 2 and 4, right panels). This offset is probably associated with the strength of cool cores that boost the cluster X-ray luminosity. Mergers also likely contribute to the scatter because the total masses can easily be incorrectly estimated when the clusters are not in hydrostatic equilibrium (HE), as happens during cluster mergers. Thus, a different sampling of the galaxy cluster population leads to observed relations that differ in both slope and normalization for the different samples. Moreover, different trends in X-ray luminosity are shown to be correlated with other X-ray observables, e.g., temperature, inducing significant covariance between cluster properties (e.g., Mantz et al. 2016; Farahi et al. 2019; Sereno et al. 2019b, 2020). Therefore, the comparison between studies with different cluster selection is very challenging. We also note that the fraction of relaxed and disturbed systems may evolve with redshift, which further complicates the comparison between local and distant samples, if the relative fraction of relaxed and disturbed systems in the sample is unknown.

Since SZ surveys are thought to be very close to being mass selected and, as such, unbiased, the different fraction of relaxed and disturbed systems in X-ray and SZ surveys also raises concerns about the representativeness of the X-ray-selected samples that are often used to define our current understanding of cluster physics and as calibration samples for numerical simulations or cosmological studies.

The Planck Early Sunyaev–Zel'dovich (ESZ; Planck Collaboration et al. 2011) cluster catalog is a good reference set for characterizing mass-selected cluster samples, for studies of structure formation including comparison with theory and simulations, and for cosmological tests. With the exception of one candidate, all the ESZ clusters have been independently confirmed (e.g., Planck Collaboration et al. 2011, 2014). Most crucially, compared to ground-based SZ surveys, which have observed only a few thousand square degrees, Planck's all-sky

($|b| > 15°$) cluster survey provides a large statistical sample spanning a broad mass range, including the rare, very massive clusters.

In Lovisari et al. (2017) several morphological parameters were derived to investigate the difference between the dynamical state of the clusters in SZ and X-ray surveys. The comparison of the Planck ESZ (Planck Collaboration et al. 2011) selected clusters with the REXCESS sample (Böhringer et al. 2007), an X-ray-selected cluster sample, indicated that the Planck clusters are, on average, less relaxed and have a lower fraction of cool core systems. This result confirmed the prediction by numerical simulations (e.g., Motl et al. 2005) and previous findings by Rossetti et al. (2016, 2017) and Andrade-Santos et al. (2017) and likely reflects the tendency of X-ray surveys to preferentially detect clusters with a centrally peaked morphology, which are more X-ray luminous at a given mass and, on average, more relaxed.

In the near future, eROSITA (Merloni et al. 2012) will provide catalogs with a large number of galaxy groups and clusters that, for the reasons outlined above, may not be representative of the whole cluster population. Thus, to fully exploit the entire eROSITA sample of detected clusters to constrain cosmological parameters, we need to take into account the different selection effects, including morphology and Malmquist or Eddington biases. While several methods (see, e.g., Pacaud et al. 2006; Pratt et al. 2009; Vikhlinin et al. 2009; Mantz et al. 2010; Lovisari et al. 2015; Schellenberger & Reiprich 2017) have been proposed to account for Malmquist and Eddington biases, little has been done to incorporate and account for the morphology bias, which is expected to be important for eROSITA (and for X-ray survey data in general). In fact, most of the clusters detected with eROSITA will have too few photons to derive gas density and temperature profiles (and thus too few to determine mass profiles). Therefore, the total masses will be mostly estimated using scaling relations (e.g., using the L–$M_{\rm tot}$ relation). Hence, cosmological studies will rely on the solid understanding of the scaling properties, for both relaxed and disturbed clusters. In addition, knowing the selection function may not be sufficient, if the scaling relations are determined using a sample that is not representative of the whole cluster population.

In this paper we derive the X-ray scaling relations for a representative sample of Planck-selected clusters and compare them with ones derived using X-ray-selected samples and for a sample of clusters detected with the South Pole Telescope (SPT; Carlstrom et al. 2011). Moreover, we investigate the scaling properties for subsamples of relaxed and disturbed clusters to highlight the impact on the relations of a different fraction of regular and dynamically active systems.

This paper is structured as follows. In Section 2 we describe the sample and the *XMM-Newton* data reduction. The determination of the X-ray properties and the methodology for quantifying the scaling relations is described in Section 3. We present our results in Section 4 and discuss them in Section 5. Section 6 contains a summary and conclusions.

Throughout this paper, we assume a flat ΛCDM cosmology with $\Omega_m = 0.3$ and $H_0 = 70\,{\rm km\,s^{-1}\,Mpc^{-1}}$. Log is always base 10 here. Uncertainties are at the 68% c.l. Several studies determined the L–$M_{\rm tot}$ and L–T relations using the luminosities in the 0.5–2 keV band instead of the 0.1–2.4 keV band used in this work. To compare these relations with our results, we corrected the normalizations, assuming a scaling factor of 1.62 obtained assuming an unabsorbed APEC model in XSPEC (Arnaud 1996) for a cluster temperature of 5 keV, an abundance of 0.3 solar, and a redshift of 0.2. The scaling factor only changes by a few percent by varying these input parameters.

2. Data

Our sample contains 120 galaxy clusters observed with *XMM-Newton* and originally selected from the Planck ESZ (Planck Collaboration et al. 2011). As described in Lovisari et al. (2017), these are the ESZ clusters for which R_{500} was completely covered by *XMM-Newton* observations, allowing the estimation of the morphological parameters. R_{500} was estimated using iteratively the M_{500}–Y_X relation given in Arnaud et al. (2010). As shown in Lovisari et al. (2017), the mass and redshift distributions of these systems are representative of the whole ESZ sample of 188 galaxy clusters.

Observation data files were downloaded from the *XMM-Newton* archive and processed with the XMMSAS (Gabriel et al. 2004) v16.0.0 software for data reduction. The initial data processing, to generate calibrated event files from raw data, was done by running the tasks *emchain* and *epchain*. We only considered single, double, triple, and quadruple events for MOS (i.e., PATTERN $\leqslant$ 12) and single events for pn (i.e., PATTERN==0), and we applied the standard procedures for bright pixels and hot column removal (i.e., FLAG==0), and pn out-of-time correction. All the data sets were cleaned for periods of high background due to the soft protons, following the two-step procedure extensively described in Lovisari et al. (2011). The point-like sources were detected with the *edetect-chain* task and visually inspected before excluding the regions with point sources from the event files. The background event files were cleaned by applying the same PATTERN selection, flare rejection, and point-source removal as for the corresponding target observations.

3. X-Ray Quantities

3.1. Luminosities

The X-ray luminosities have been derived within two different apertures: 0–1R_{500} (referred to as core-excised luminosity). The total count rates within the different apertures have been derived by integrating the surface brightness (SB) derived in the 0.3–2 keV band and then converted into the 0.1–2.4 keV band (hereafter $L_{\rm X}$) and bolometric (i.e., 0.01–100 keV band, hereafter $L_{\rm bol}$) luminosities with XSPEC, using the best-fit spectral model estimated in the same aperture. Uncertainties take into account both the statistical factors and the uncertainties in the derivation of R_{500}. The relative errors were estimated via Monte Carlo realizations by randomly varying the observational data points of the SB profiles to determine a new best fit. The randomization was performed assuming a Gaussian distribution with mean and standard deviation equal to the observed uncertainties.

3.2. Temperatures

Spectroscopic temperatures have been obtained by fitting the spectra with an APEC thermal plasma model with an absorption fixed at the total (neutral and molecular; see Willingale et al. 2013) $N_{\rm H}$ value estimated using the SWIFT online tool,[5] with the exception of a few clusters (marked with

[5] http://www.swift.ac.uk/analysis/nhtot/index.php

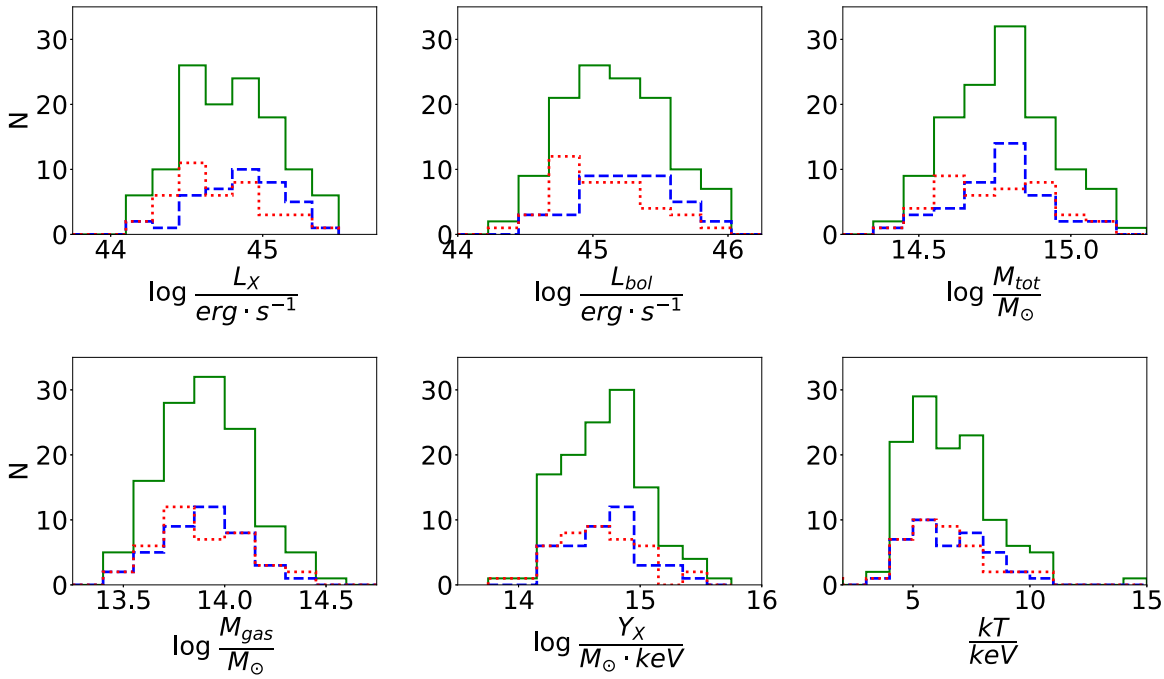

Figure 1. Distribution of soft-band luminosity (0.1–2.4 keV) L_X (top left), bolometric luminosity (0.01–100 keV) L_{bol} (top middle), total mass M_{tot} (top right), gas mass M_{gas} (bottom left), $Y_X = M_{gas} \times kT$ (bottom middle), and temperature kT (bottom right) of the ESZ sample of galaxy clusters observed with *XMM-Newton*. The distribution of the full sample is shown in green, while the distribution of the most relaxed (1/3 of the total) and most disturbed (1/3 of the total) clusters is shown in blue and red, respectively.

a star in Table 3), which were found to have a significantly different absorption than the value indicated from the tool. All MOS and pn spectra were fitted simultaneously in the full (i.e., 0.3–10 keV) energy band, with temperature and abundance linked, while the normalizations were left free to vary to account for the different cross-calibration between the detectors (see, e.g., Schellenberger et al. 2015). The modeling of the background is described in Lovisari & Reiprich (2019).

The radial temperature profiles have been derived by extracting the spectra from successive annular regions created around the X-ray peak. We required a minimum width of 30″ to ensure that the redistribution fraction of the flux is at most about 20% (Zhang et al. 2009) and a signal-to-noise ratio $\geqslant 50$ to ensure an uncertainty of ∼10% in the spectrally resolved temperature (and consequently in the fitted temperature profiles). We also required the source-to-background count rate ratio to be higher than 0.6 to reduce the systematic uncertainties in the temperature measurements (see Leccardi & Molendi 2008 for more details). The number of obtained bins per cluster is listed in Table 3. The profiles are then deprojected, using the method presented in Vikhlinin (2006). The implementation has been done following Schellenberger & Reiprich (2017), where the parameters of the deprojected temperature profile are determined using a Markov Chain Monte Carlo. The input temperature profiles are projected along the line of sight at every radius that has a measurement and compared to the observed profile, until convergence. Then, the global and core-excised temperatures, used in the scaling relations, were determined by integrating the deprojected profiles along the line of sight (starting from the center and $0.15R_{500}$, respectively) weighted by the emission measure and accounting for the detector response. We verified that these temperatures are in good agreement with the temperatures derived using a single spectral extraction: a linear fit gives a slope of 0.97 ± 0.03 and an intrinsic scatter of ∼6%. It should be noted that not only uncertainties in the 3D temperature profile parameters but also all MCMC chains are used for the following steps (e.g., calculating the total mass), to assure that the covariance of parameters is taken into account.

3.3. Masses

The total cluster masses can be obtained by solving the HE equation. Assuming spherical symmetry, the total cluster mass M within a radius r is given by

$$M(<r) = -\frac{rk_B T}{G\mu m_p}\left\{\frac{d\ln\rho}{d\ln r} + \frac{d\ln T}{d\ln r}\right\}, \quad (1)$$

where k_B and G are the Boltzmann and gravitational constants, respectively, and μ is the mean particle weight in units of the proton mass m_p. The observational inputs needed for this calculation are the density profiles obtained in Lovisari et al. (2017) and the temperature profiles obtained as discussed in Section 3.2. We solved Equation (1) for the radii of the spectral extraction regions (temperature measurements) and fitted a Navarro–Frenk–White model (Navarro et al. 1997) up to the outer regions for the mass profile with the relation from Bhattacharya et al. (2013) between the dark matter concentration c_{500} and R_{500} as a prior, which constrains the posterior distribution of R_{500} to reasonable values (see Schellenberger & Reiprich 2017 for more details). The mass of the gas is then calculated by integrating the density profile within R_{500} estimated from Equation (1), and, together with the cluster temperature, it is used to determine the $Y_X (= M_{gas} \times kT)$ and $Y_{X,exc} (= M_{gas} \times kT_{exc})$ parameters. The derived properties for individual clusters are listed in Table 3, and their distribution is shown in Figure 1.

Table 1
Self-similar Values and Pivot Points Used in the Scaling Relations in the Form of $Y \propto E_z^{\gamma} X^{\beta}$

Relation (Y, X)	$\gamma_{\rm self}$	$\beta_{\rm self}$	$C1$	$C2$
$L_{\rm X}$–$M_{\rm tot}$	2	1	5×10^{44} erg s^{-1}	$6 \times 10^{14}\ M_{\odot}$
$L_{\rm X}$–T	1	3/2	5×10^{44} erg s^{-1}	5 keV
$L_{\rm bol}$–$M_{\rm tot}$	7/3	4/3	1×10^{45} erg s^{-1}	$6 \times 10^{14}\ M_{\odot}$
$L_{\rm bol}$–T	1	2	1×10^{45} erg s^{-1}	5 keV
$M_{\rm tot}$–T	−1	3/2	$6 \times 10^{14}\ M_{\odot}$	5 keV
$M_{\rm tot}$–$Y_{\rm X}$	−2/5	3/5	$6 \times 10^{14}\ M_{\odot}$	$5 \times 10^{14}\ M_{\odot}$ keV
$M_{\rm tot}$–$M_{\rm gas}$	0	1	$6 \times 10^{14}\ M_{\odot}$	$10^{14}\ M_{\odot}$

Note. In the second and third columns we provide the predictions from the self-similar scenario for the redshift evolution $\gamma_{\rm self}$ and scaling relation slope $\beta_{\rm self}$, respectively. *C1* and *C2* values are the pivot points used in Equation (2).

4. Fitting the Scaling Relations

We investigated the following relations: L–$M_{\rm tot}$, L–T, $M_{\rm tot}$–T, $M_{\rm tot}$–$Y_{\rm X}$, and $M_{\rm tot}$–$M_{\rm gas}$. We fitted the relations using both the soft-band (0.1–2.4 keV) and bolometric luminosities (0.01–100 keV), as well as both the global and core-excised properties, when appropriate. The full uncertainty covariance matrix between the X-ray properties was computed and used for the analysis of the scaling relations. For each set of parameters (X, Y), we linearly fit our data as

$$\log\left(\frac{Y}{C1}\right) = \alpha + \beta \log\left(\frac{Z}{C2}\right) + \gamma \log F_z \pm \sigma_{Y|Z} \log X = \log Z \pm \sigma_{X|Z}, \quad (2)$$

where Z is the intrinsic cluster property (i.e., the "true" quantity), α the normalization, β the slope, γ the evolution with redshift, σ the intrinsic scatter[6] in the two variables X and Y, and $F_z = E_z/E_{z,\rm ref}(z_{\rm ref} = 0.2)$. $E_z = H_z/H_0 = [\Omega_m(1+z)^3 + \Omega_\Lambda]^{0.5}$ indicates the dependence on the evolution of the *Hubble* constant at redshift z. The pivot points, *C1* and *C2*, have been chosen to be roughly the median values of the sample, and they are summarized in Table 1. For each relation, we also provide the predicted slope $\beta_{\rm self}$ and redshift evolution $\gamma_{\rm self}$ in the case where gravity is the dominant process, a scenario that is referred to as the self-similar model (see, e.g., Maughan et al. 2012).

We fit the data with a linear relation of the variables in log space using the R-package LIRA.[7] LIRA is based on a Bayesian method that can deal with heterogeneous data and correlated errors and allow normalizations, slopes, and scatters (and relative uncertainties) to be fitted simultaneously (see Sereno 2016 for more details). As a default, all the important parameters are left free to vary, and central values and uncertainties are summarized in Table 2 (and a visual recap of all β, γ, and σ is presented in Section 6; see Figures 8 and 10). The impact of freezing some of the parameters is discussed in Appendix B, where, for comparison, we also provide the central values obtained using the routine LINMIX by Kelly (2007) and the best-fit values from *BCES* by Akritas & Bershady (1996), and we discuss the resulting differences. To allow the reader to reproduce our results, in Appendix C, we provide the LIRA commands to be used in the different cases investigated in this paper.

In Table 2, we also provide an estimate of the goodness of the fit, computed as

$$C_{\rm gof} = \frac{1}{N_{\rm cl}} \sum_{i}^{N_{\rm cl}} \frac{(y_i - \alpha - \beta x_i - \gamma \log F_z)^2}{\delta_{y,i}^2 + \sigma_{Y|Z}^2 + \beta^2(\delta_{x,i}^2 + \sigma_{X|Z}^2) - 2\beta\delta_{xy,i}}, \quad (3)$$

where δ_x and δ_y denote the statistical uncertainties and δ_{xy} is the uncertainty covariance. This term gives an idea of the goodness of fit, but it does not follow a (reduced) χ^2 statistic. In fact, the intrinsic scatters $\sigma_{X|Z}$ and $\sigma_{Y|Z}$ are estimated in the regression procedure and are not known a priori. Furthermore, $C_{\rm gof}$ is computed for the mean values of the parameter posterior distribution and not for the maximum likelihood parameters.

5. Results

To investigate the impact of the cluster dynamical state on the scaling relations, we used the morphological information (i.e., centroid-shift and concentration parameter) from Lovisari et al. (2017) to select the most relaxed "R" (1/3 of the total) and most disturbed "D" (1/3 of the total) clusters in the ESZ sample. Their distribution is also shown in Figure 1. In the following we discuss the individual scaling relation results for the full ESZ sample and for the subsamples of relaxed and disturbed clusters.

5.1. $L_{\rm X}$–M_{tot}

In Figure 2 we show the results for the $L_{\rm X}$–$M_{\rm tot}$ relation. The relation is corrected for the Eddington bias (see Sereno 2016 for more details), but not for the Malmquist bias, which is negligible[8] when fitting the X-ray properties of an SZ-selected sample. The fitted relation is shown with a solid green line, while the dark green shaded area encloses the 1σ confidence region around the median scaling relation. We also show the bias-corrected relations derived for well-known X-ray-selected samples: REXCESS (Pratt et al. 2009, hereafter GP09), HIFLUGCS (Schellenberger & Reiprich 2017, hereafter GS17), 400d (Vikhlinin et al. 2009, hereafter AV09), and the flux-limited samples of massive clusters by Mantz et al. (2010, hereafter AM10) and Mantz et al. (2016, hereafter AM16). Moreover, we show the recent result from Bulbul et al. (2019, hereafter EB19), who investigated the X-ray properties of a sample of SPT clusters spanning the redshift range from $z = 0.2$ to $z = 1.5$.

We find a relation steeper than the prediction of the self-similar scenario (i.e., $\beta > 1$), which is probably the result of the combined effect of gas cooling, active galactic nucleus (AGN) feedback, and subcluster mergers. We also find mild evidence for negative redshift evolution (i.e., $\gamma < 1$), in agreement with Sereno & Ettori (2015b). This might be a sign

[6] The intrinsic scatter manifests as a data distribution around a relation. Therefore, the smaller the intrinsic scatter value is, the closer the data distribution is to strict linearity. In LIRA, the intrinsic scatter refers to the probability of the variable of interest (X when $\sigma_{X|Z}$ is considered, or Y in the case of $\sigma_{Y|Z}$) given the latent property Z (e.g., the true cluster mass).

[7] LIRA (LInear Regression in Astronomy) is available from the R archive network at https://cran.r-project.org/web/packages/lira/index.html.

[8] In a forthcoming paper by Andrade-Santos et al. we will show that, indeed, the Malmquist bias is not important for the present SZ-selected samples.

Table 2
Fitted Relations for the ESZ Sample

Relation (Y–X)	Subsample	α	β	γ	$\sigma_{X\|Z}$	$\sigma_{Y\|Z}$	$C_{\rm gof}$
$L_{\rm X}$–$M_{\rm tot}$	all	0.089 ± 0.015	1.822 ± 0.246	0.462 ± 0.916	0.061 ± 0.021	0.082 ± 0.040	1.09
	relaxed	0.162 ± 0.022	1.756 ± 0.243	0.323 ± 1.058	0.061 ± 0.022	0.066 ± 0.040	1.04
	disturbed	0.050 ± 0.029	1.551 ± 0.272	0.571 ± 1.053	0.049 ± 0.024	0.102 ± 0.041	1.01
$L_{\rm X,exc}$–$M_{\rm tot}$	all	-0.091 ± 0.013	1.668 ± 0.183	1.325 ± 0.804	0.063 ± 0.015	0.034 ± 0.029	1.03
	relaxed	-0.092 ± 0.018	1.589 ± 0.196	1.357 ± 1.154	0.055 ± 0.016	0.038 ± 0.026	1.06
	disturbed	-0.056 ± 0.027	1.524 ± 0.264	0.738 ± 1.051	0.053 ± 0.023	0.080 ± 0.038	1.03
$L_{\rm bol}$–$M_{\rm tot}$	all	0.174 ± 0.016	2.079 ± 0.230	0.541 ± 0.904	0.050 ± 0.020	0.098 ± 0.042	1.10
	relaxed	0.254 ± 0.023	2.085 ± 0.235	0.337 ± 1.064	0.051 ± 0.019	0.074 ± 0.043	1.04
	disturbed	0.134 ± 0.031	1.868 ± 0.265	0.375 ± 1.025	0.046 ± 0.022	0.106 ± 0.046	1.01
$L_{\rm bol,exc}$–$M_{\rm tot}$	all	-0.006 ± 0.014	1.921 ± 0.189	1.561 ± 0.848	0.052 ± 0.016	0.050 ± 0.034	1.07
	relaxed	0.003 ± 0.020	1.962 ± 0.202	1.222 ± 1.174	0.048 ± 0.015	0.039 ± 0.030	1.02
	disturbed	0.027 ± 0.028	1.787 ± 0.264	0.814 ± 1.097	0.046 ± 0.022	0.091 ± 0.041	1.03
$L_{\rm X}$–T	all	-0.250 ± 0.045	3.110 ± 0.422	0.398 ± 0.939	0.051 ± 0.010	0.052 ± 0.041	1.08
	relaxed	-0.133 ± 0.045	2.703 ± 0.380	0.114 ± 1.044	0.040 ± 0.013	0.079 ± 0.041	1.02
	disturbed	-0.257 ± 0.043	2.593 ± 0.418	1.127 ± 1.067	0.036 ± 0.013	0.071 ± 0.037	1.38
$L_{\rm X,exc}$–$T_{\rm exc}$	all	-0.360 ± 0.031	2.409 ± 0.292	1.170 ± 0.822	0.038 ± 0.011	0.052 ± 0.031	1.13
	relaxed	-0.365 ± 0.026	2.350 ± 0.194	1.166 ± 0.838	0.026 ± 0.007	0.030 ± 0.018	1.13
	disturbed	-0.341 ± 0.041	2.525 ± 0.418	1.213 ± 1.084	0.035 ± 0.013	0.070 ± 0.035	1.39
$L_{\rm bol}$–T	all	-0.209 ± 0.044	3.464 ± 0.400	0.661 ± 0.964	0.044 ± 0.010	0.061 ± 0.045	1.10
	relaxed	-0.104 ± 0.047	3.250 ± 0.383	0.068 ± 1.088	0.034 ± 0.011	0.082 ± 0.044	1.00
	disturbed	-0.241 ± 0.042	3.134 ± 0.386	1.042 ± 1.043	0.032 ± 0.011	0.066 ± 0.039	1.35
$L_{\rm bol,exc}$–$T_{\rm exc}$	all	-0.324 ± 0.027	2.808 ± 0.247	1.496 ± 0.757	0.030 ± 0.009	0.054 ± 0.030	1.12
	relaxed	-0.341 ± 0.027	2.924 ± 0.198	0.920 ± 0.839	0.021 ± 0.006	0.030 ± 0.019	1.04
	disturbed	-0.315 ± 0.039	3.022 ± 0.387	1.423 ± 1.094	0.031 ± 0.010	0.056 ± 0.034	1.37
$M_{\rm tot}$–T	all	-0.171 ± 0.015	1.556 ± 0.137	0.179 ± 0.379	0.032 ± 0.010	0.036 ± 0.016	1.03
	relaxed	-0.172 ± 0.020	1.556 ± 0.157	-0.188 ± 0.582	0.027 ± 0.010	0.040 ± 0.017	0.96
	disturbed	-0.191 ± 0.026	1.610 ± 0.250	0.414 ± 0.642	0.036 ± 0.012	0.039 ± 0.020	1.09
$M_{\rm tot}$–$T_{\rm exc}$	all	-0.165 ± 0.014	1.508 ± 0.126	0.235 ± 0.370	0.026 ± 0.009	0.043 ± 0.015	1.02
	relaxed	-0.178 ± 0.019	1.536 ± 0.138	-0.243 ± 0.549	0.025 ± 0.009	0.037 ± 0.015	0.97
	disturbed	-0.180 ± 0.026	1.616 ± 0.259	0.329 ± 0.633	0.035 ± 0.013	0.046 ± 0.022	1.10
$M_{\rm tot}$–$M_{\rm gas}$	all	0.073 ± 0.007	0.802 ± 0.049	-0.317 ± 0.307	0.028 ± 0.015	0.043 ± 0.011	1.04
	relaxed	0.080 ± 0.008	0.864 ± 0.047	-0.801 ± 0.411	0.025 ± 0.010	0.027 ± 0.009	1.32
	disturbed	0.064 ± 0.022	0.800 ± 0.127	-0.063 ± 0.664	0.054 ± 0.027	0.055 ± 0.021	1.01
$M_{\rm tot}$–$Y_{\rm X}$	all	-0.010 ± 0.005	0.540 ± 0.030	-0.292 ± 0.287	0.039 ± 0.023	0.039 ± 0.011	1.00
	relaxed	-0.010 ± 0.007	0.561 ± 0.034	-0.635 ± 0.428	0.034 ± 0.019	0.031 ± 0.010	1.09
	disturbed	-0.019 ± 0.013	0.538 ± 0.069	-0.043 ± 0.568	0.066 ± 0.037	0.049 ± 0.019	0.96
$M_{\rm tot}$–$Y_{\rm X,exc}$	all	-0.008 ± 0.005	0.534 ± 0.031	-0.257 ± 0.289	0.039 ± 0.024	0.040 ± 0.011	1.03
	relaxed	-0.012 ± 0.007	0.558 ± 0.033	-0.639 ± 0.424	0.036 ± 0.019	0.030 ± 0.010	1.12
	disturbed	-0.014 ± 0.013	0.539 ± 0.072	-0.062 ± 0.580	0.069 ± 0.038	0.050 ± 0.019	1.01

Note. The subsample of relaxed (disturbed) clusters have an SB concentration higher (lower) than 0.18 and a centroid-shift lower (higher) than 0.0137. The morphological parameter values have been taken from Lovisari et al. (2017). The definition of $C_{\rm gof}$ is given in Equation (3).

of additional radiative cooling and uniform (pre)heating at high redshift.

There is good agreement between the slopes determined using Planck- and SPT-selected samples, despite the different distributions of cluster masses and redshifts (i.e., the SPT-selected clusters used by EB19 are on average at higher redshift and lower mass than the ones used in our work). However, there is a normalization offset on the order of $\sim$45% at $M_{\rm tot} = 6 \times 10^{14}\,M_{\odot}$ and $z = 0.2$ between the two relations, which reduces to $\sim$23% when self-similar redshift evolution (i.e., $\gamma = 2$) is assumed. A large offset in the scaling relations is also observed when comparing our results with those derived from the X-ray-selected samples, with the exception of the REXCESS sample, which instead agrees extremely well with our results. However, as noted by AM16, a straightforward comparison between the different studies is difficult because the total masses have been derived using different methods (e.g., AV09 and GS17 used the HE equation, while GP09 and AM10 used, respectively, $Y_{\rm X}$ and $M_{\rm gas}$ as a proxy). Nonetheless, we note that the flux-limited samples (GS17, AM10, and AM16) show flatter relations than all the other samples. The X-ray samples used by GP09 and AV09,

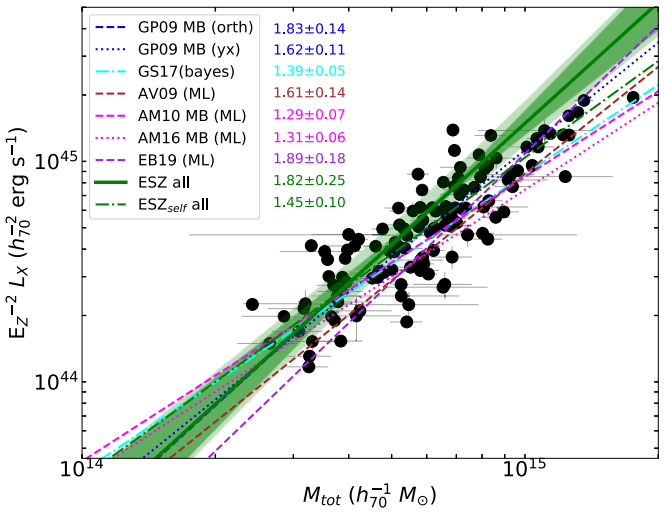

Figure 2. Comparison of the L_X–M_{tot} relation determined in this work (green lines) with the bias-corrected relations obtained with well-studied samples selected in both X-ray and SZ. L_X are the soft-band (0.1–2.4 keV) luminosities. The full green line represents the fitted scaling relation with the time evolution free to vary in the fit. The dark and light shaded areas represent the 1σ statistical error and scatter, respectively. The dashed–dotted green line represents the fitted relation assuming self-similar redshift evolution. The slopes of the relations derived from the X-ray-selected samples, with the exception of GP09, are flatter than those from relations derived using SZ-derived samples (i.e., ESZ and EB19). For the acronyms in the legend see Section 5.1.

which have properties of both a flux- and a volume-limited sample, have slopes for the derived scaling relations in better agreement with the results obtained from SZ-selected clusters.

If we force the redshift evolution to be self-similar (i.e., $\gamma = 2$), similar to what was done by, e.g., GS17, we find a flatter relation for the ESZ sample, more in agreement with GS17 results. As discussed in Appendix B, fixing the redshift evolution impacts our relations by changing both slope and normalization.

In Figure 3 (top panel), we show the distribution of the relaxed (in blue) and disturbed (in red) clusters, with respect to the fitted relation for the full sample (green line), along with the relations found in earlier studies. We found that relaxed clusters have, on average, higher soft-band (0.1–2.4 keV) luminosities L_X than disturbed systems, confirming the finding by GP09. Thus, when the relaxed and disturbed subsamples are fitted independently, we find that they have similar slopes (only slightly flatter for the disturbed clusters) but different intrinsic scatter and normalizations. The intrinsic scatter is only $\sim$16% for the relaxed systems, while it is significantly larger, $\sim$26%, for the disturbed clusters. The relatively low scatter observed for the relaxed clusters is probably due to the fact that the dominant contribution to the scatter for these systems is the presence of a dense core that scatters L_X always in the same direction (i.e., boost of L_X). On the contrary, in disturbed clusters there are many processes (e.g., nonthermal pressure, substructures and clumps, shocks and temperature inhomogeneities) playing a role, each of them acting in different directions and with a different magnitude.

At $M_{tot} = 6 \times 10^{14}\,M_\odot$ and $z = 0.2$ the normalization of the relation for the most relaxed clusters is $\sim$20% higher than the relation fitted if we included all the objects. The normalization of the relation for the most disturbed clusters is, instead, $\sim$10% lower than the relation fitted including all the objects. This implies that, for a given total cluster mass, the X-ray soft-band luminosity of disturbed galaxy clusters is on average $\sim$30% lower than the luminosity of relaxed clusters. That means that if we do not take into account the dynamical state information for the X-ray-selected samples, which are biased toward relaxed systems, we are not able to properly correct for all the selection biases. Indeed, this poses an issue for the eROSITA studies, because there will be too few counts to determine their cluster morphology or to derive accurate core-excised X-ray properties. Assuming that SZ-selected samples better represent the true cluster population, one can use them to correct the scaling relations derived with X-ray-selected samples and/or calibrate different mass proxies.

5.2. $L_{X,exc}$–M_{tot}

Several studies have shown that using the core-excised luminosities helps to reduce the scatter of the L_X–M_{tot} relation (e.g., Pratt et al. 2009; Mantz et al. 2018). Therefore, we also computed the X-ray soft-band luminosities L_X, excluding the core, corresponding to $0.15R_{500}$. Indeed, these relations show a much lower scatter with respect to those derived using luminosities with the cores included. The intrinsic scatter reduction is more significant for the most relaxed clusters, in agreement with the idea that the dominant contribution to the scatter for these systems is the dense and peaked core, while for disturbed systems different processes, not associated with the core, are responsible for the scatter. The relations determined with core-excised luminosities are moderately flatter, but consistent within uncertainties, than the ones with the core-included ($\beta = 1.668 \pm 0.183$ vs. $\beta = 1.822 \pm 0.246$), which may suggest a larger fraction of relaxed clusters at high masses. However, the same effect (i.e., flattening of the slope) is less obvious when fitting the data assuming the redshift self-similar evolution (i.e., $\gamma = 2$). That could be explained if relaxed and disturbed systems evolve differently with redshift. Although the large uncertainties in γ, due to the limited redshift range of our sample, do not allow conclusive results, we have indeed hints of a slightly larger negative evolution for the most relaxed clusters (i.e., the fitted γ for relaxed clusters tends to be systematically lower than the γ derived for disturbed systems; see Table 2 and Figure 8). Moreover, when using the core-excised properties, we note a systematic trend to higher γ values that is in better agreement with the self-similar predictions.

Using the core-excised luminosities, we find that relaxed and disturbed systems share very similar relations. This agreement suggests that, independently of the relative fraction of relaxed and disturbed systems in a sample, the core-excised luminosities can be used to obtain a universal relation that can be used for future surveys. However, we note that core-excised temperatures usually cannot be measured for poor clusters or groups even in relatively deep surveys like XXL (e.g., Pierre et al. 2016). Moreover, although the use of the L_{exc} helps to reduce the offset between the different relations for X-ray- and SZ-selected samples, there is still a normalization offset that requires the determination of the true cluster mass scale (see the review by Pratt et al. 2019) to obtain the universal $L_{X,exc}$–M_{tot} relation (in the case of AM10 there is also a difference in the slope, which may depend on the different proxy used to

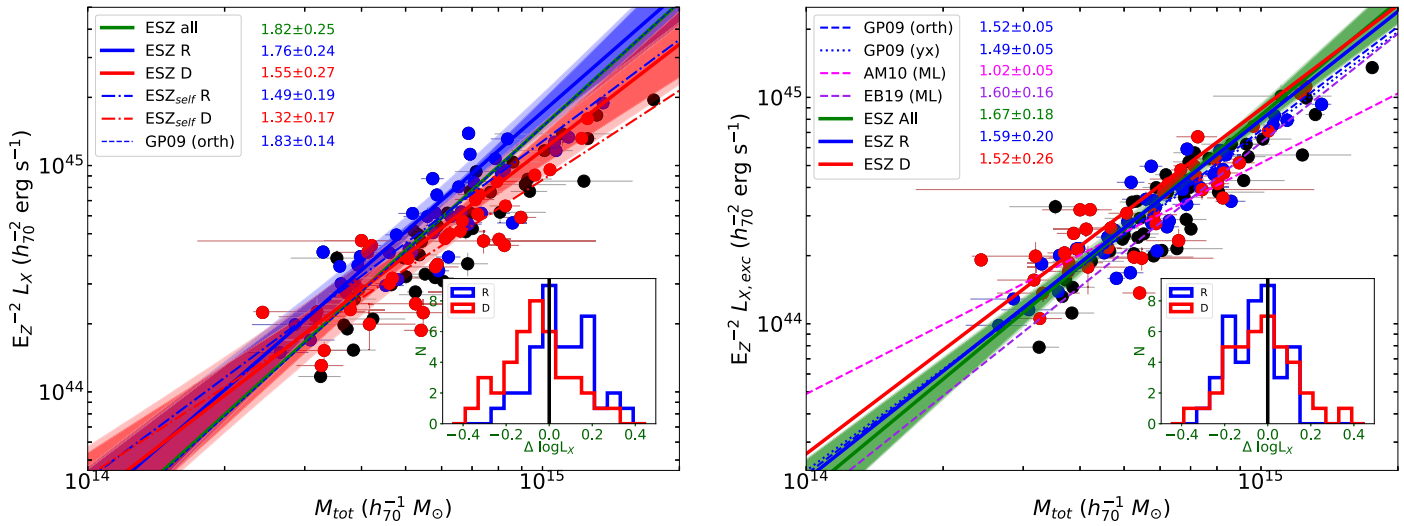

Figure 3. Left: L_X–M_{tot} relations determined for relaxed (blue) and disturbed (red) systems independently. Clusters that are not classified in either of the two subsamples are shown in black. The green line shows the fitted relation for all the clusters. The relations obtained with the redshift evolution frozen to the self-similar value, $\gamma = 2$, are indicated with a "self" subscript. In the inset plot we show the histogram of the log space residuals from the fitted L_X–M_{tot} relation, derived with γ free to vary. Relaxed clusters are, on average, above the relation, while disturbed clusters are, on average, below. Right: comparison of the $L_{X,exc}$–M_{tot} relation determined in this work with some of the relations available in the literature. Using the core-excised luminosities brings into better agreement the relations of relaxed and disturbed clusters. The histogram of the log space residuals in the inset plot shows that relaxed and disturbed systems are distributed around the fitted relation when core-excised luminosities are used. L_X are soft-band (0.1–2.4 keV) luminosities. For the acronyms in the legend see Section 5.1.

estimate the total masses). In Figure 3 (right panel) we show the $L_{X,exc}$–M_{tot} relation showing good agreement between all the relations.

5.3. L_{bol}–M_{tot} and $L_{bol,exc}$–M_{tot}

The relations of the ESZ sample determined using the bolometric luminosities (i.e., 0.01–100 keV) L_{bol} are steeper than those found using the luminosities in the soft X-ray band (i.e., 0.1–2.4 keV). The slope is steeper than the prediction from the self-similar scenario with a significance of more than 3σ, using both core-excised and core-included luminosities. Similarly to the L_X–M_{tot} relation, we observe hints of a negative evolution (i.e., $\gamma = 0.541 \pm 0.940$) with respect to the self-similar scenario (i.e., $\gamma = 7/3$). The intrinsic scatter, larger than the one obtained using the soft-band luminosities, is at the ∼25% level, and it is comparable to others found in the literature (e.g., EB19). Again, the scatter is larger for the disturbed clusters, and the reduction, after removing the cores, is larger for the most relaxed systems.

5.4. L_X–T and $L_{X,exc}$–T_{exc}

Because of the different methods used to determine the total cluster mass (HE, WL, mass proxies, etc.), comparing the L–M_{tot} relations from different studies is not always straightforward and can potentially bias our interpretation of the impact on the scaling relations of the different selection effects (e.g., the different fractions of relaxed/disturbed clusters). A more direct comparison can be done using the L–T relation, although cross-calibration uncertainties between *Chandra* and *XMM-Newton* should be taken into account. While at low intracluster medium (ICM) temperatures both observatories deliver similar results, the differences increase in the high-temperature regime (see Schellenberger et al. 2015, for more details), where most of our clusters reside.

In Figure 4 (left panel), we compare our result with the finding by GP09, Lovisari et al. (2015, hereafter LL15), Giles et al. (2016, hereafter XXL), and Migkas[9] et al. (2020, hereafter KM20).

The L_X–T relation is significantly steeper than the value predicted by the self-similar scenario (i.e., $\beta = 3.110 \pm 0.422$ vs. $\beta = 1.5$). Although the fit prefers a slightly smaller redshift evolution factor γ (but consistent within the uncertainties with the self-similar prediction), the impact on the slope is quite small. Similarly to the L_X–M_{tot} relation, we observe quite good agreement for the L_X–T relation with other works for the slope but a significant offset for the normalization. Again, the most relaxed clusters tend to have a higher luminosity for a given temperature (see Figure 4, left panel). At 5 keV, relaxed clusters have, on average, a luminosity ∼50% higher than disturbed clusters.

The use of the core-excised luminosities brings into better agreement the best-fit relations for relaxed and disturbed clusters (see Figure 4, right panel). The $L_{X,exc}$–T_{exc} relation, although shallower than the L_X–T relation, is still much steeper than what is predicted by the self-similar scenario ($\beta = 1.5$). The slope determined by AM10 is only slightly flatter than other results and can be easily explained by the higher temperatures delivered by *Chandra* used by AM10 compared to those from *XMM-Newton* used in this work and GP09.

The scatter of the temperature is smaller than the scatter of the total mass, indicating that the temperature is less sensitive than the total mass to the processes (e.g., presence of substructures) affecting the scatter. The results for the L_X–T relation confirm that scatter in L_X is basically driven by the

[9] KM20 used an eeHIFLUGCS-like sample (see Reiprich 2017) to determine the L_X–T relation. When available, the *Chandra* data were used to determine the cluster temperature, while *XMM-Newton* observations have been used for clusters not observed with *Chandra* (i.e., roughly one-third of the sample). For the comparison with our results, we converted the *Chandra* temperatures to *XMM*-like temperatures, using the equation determined by Schellenberger et al. (2015).

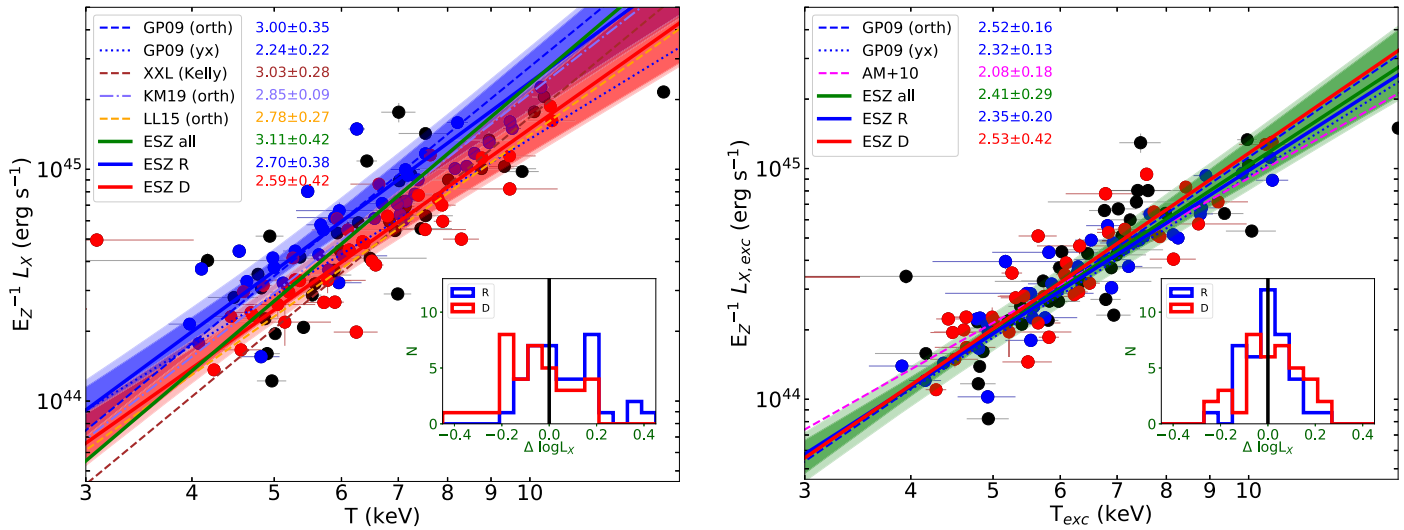

Figure 4. Left: comparison of the L_X–T relation determined in this work with the best-fit relations obtained from other well-studied samples selected in the X-ray. L_X are soft-band (0.1–2.4 keV) luminosities. The green line represents the fitted relation with γ free to vary in the fit. The dark and light shaded areas represent the 1σ statistical error and scatter, respectively. In blue and red we show the fitted relations determined for relaxed and disturbed systems, independently. In the inset plot, we show the histogram of the log space residuals from the fitted L_X–T relation. As for the L_X–M_{tot} relation (see Figure 3), relaxed objects are on average above the relation, while disturbed clusters are on average below. Right: comparison of the $L_{X,exc}$–T_{exc} relation determined in this work with some of the relations available in the literature. The histogram of the log space residuals in the inset plot shows that relaxed and disturbed clusters distribute homogeneously around the fitted relation, when core-excised luminosities and temperatures are used. The acronyms in the legend are described in Sections 5.1 and 5.4.

boost in luminosity due to the peaked cores. In fact, we do not see any reduction of the scatter for the L–T relation of the most disturbed clusters derived using the core-excised luminosities, either in $\sigma_{Y|Z}$ or $\sigma_{Y|Z}$. The lower scatter of the L–T relation can also be caused by positively correlated intrinsic scatter of luminosity and temperature at a given mass (Mantz et al. 2016; Sereno et al. 2019a).

5.5. L_{bol}–T *and* $L_{bol,exc}$–T_{exc}

As was the case with soft X-ray luminosities, the L–T relations obtained with the bolometric luminosities have a slope significantly steeper than the self-similar scenario (i.e., $\beta = 3.464 \pm 0.400$ vs. $\beta = 2$). Although the core-excised temperatures and luminosities help to flatten the slope (i.e., $\beta = 2.808 \pm 0.247$), this is not sufficient to bring it into agreement with self-similar expectations (i.e., $\beta = 2$). In both cases, the redshift evolution of the full sample is in agreement with the predicted evolution (i.e., $\gamma = 1$). However, when using the core-included L_{bol} and T, the evolution of the most relaxed objects deviates at the $\sim 1\sigma$ level from the prediction, while that is not the case for the disturbed systems. Again, using the core-excised luminosities helps to reduce the scatter for the subsample of relaxed clusters, but it has little effect on the subsample of disturbed systems (see Table 2).

5.6. M_{tot}–M_{gas}

The mass of the ICM correlates very well with the total cluster mass with a relatively small intrinsic scatter (e.g., Okabe et al. 2010; Lovisari et al. 2015; Sereno et al. 2019b). Moreover, the M_{gas} computed with *Chandra* and *XMM-Newton* within the same radius agree within a few percent (e.g., Bartalucci et al. 2017). In Figure 5, we show that this is indeed also the case for the ESZ sample. Moreover, we note that the slopes of fits to the different samples are in quite good agreement. Since the fraction of relaxed and disturbed systems in these samples is quite different, this implies that the slope of

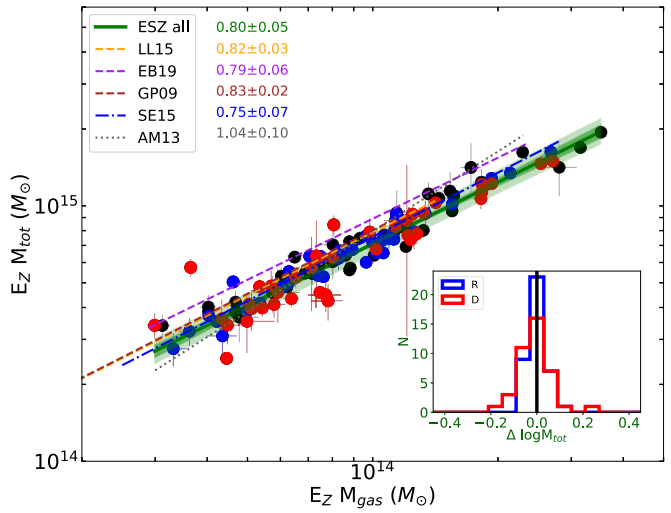

Figure 5. M_{tot}–M_{gas} relation for the ESZ clusters investigated in this work. The most relaxed and most disturbed clusters are shown in blue and red, respectively. The green line represents the fitted relation with γ free to vary in the fit. The dark and light shaded areas represent the 1σ statistical error and scatter, respectively. All the relations are plotted only in the mass range covered by the individual study. In the inset plot, we show the histogram of the log space residuals from the fitted M_{tot}–M_{gas} relation. The agreement between the slopes obtained with samples having a different fraction of relaxed and disturbed systems and between the subsamples of relaxed and disturbed clusters in the ESZ sample suggests that this relation is insensitive to the dynamical state of the clusters. However, the offset observed in the normalization may suggest that the mass range of the investigated samples plays a role because of the increasing gas fraction for high-mass systems. The acronyms in the legend are described in Sections 5.1, 5.4, and 5.6.

the M_{tot}–M_{gas} relation is quite insensitive to the dynamical state of the clusters. This is indeed confirmed by the results for the subsamples of relaxed and disturbed systems, which show a good agreement in their slopes, although the intrinsic scatter for the disturbed clusters is larger than the one for relaxed clusters. The higher scatter observed in disturbed systems for both M_{tot}

and $M_{\rm gas}$ is not surprising given the assumption of spherical symmetry. In fact, for these systems the presence of substructures and large-scale inhomogeneities may bias the reconstruction of the clusters' properties (e.g., Vazza et al. 2013; Zhuravleva et al. 2013).

There is an offset in the normalization, of the order of 5% at $10^{14}\,M_{\odot}$ and $z = 0.2$, between the relations obtained in this work and the results from Ettori (2015, hereafter SE15). The offset is even larger, of the order of 10% if compared with GP09 and LL15, and of the order of 20% with EB19. Part of this offset can be attributed to the nature of the different samples (i.e., ESZ contains more disturbed clusters), as shown by the better agreement between the ESZ relaxed clusters and the X-ray-selected samples. This is because the normalization of the relaxed clusters is ∼4%–5% higher than the one for the disturbed clusters. Moreover, the lower mass range covered by the other samples (see Figure 5), with respect to the ESZ sample, may also play a role. In fact, low-mass systems have a lower gas fraction than the most massive ones (e.g., Vikhlinin et al. 2006; Pratt et al. 2009; Lovisari et al. 2015), implying a lower gas mass for a given cluster mass than what one would expect if the gas fraction were universal, and linearly related to the total mass. Thus, samples skewed toward massive systems, where the effects of baryonic processes and radiative cooling are expected to be relatively less impactful, are expected to have a lower normalization in the $M_{\rm tot}$–$M_{\rm gas}$ plane. To support this interpretation, in Figure 5 we only plot the relations in the mass range investigated in the individual papers, and we can see that, with the exception of EB19, there is a shift toward lower normalizations in the $M_{\rm tot}$–$M_{\rm gas}$ plane when only massive clusters are considered. Apart from the best-fit relation from Mahdavi et al. (2013, hereafter AM13), all the other relations point to a slope close to ∼0.8, therefore flatter than what is predicted if the gas fractions were the same on all mass scales. The agreement between the slopes, but not in the normalization, suggests that this relation is almost independent of the fraction of relaxed and disturbed systems in the sample but may depend on the mass range of the clusters that are investigated or on systematic differences in HE mass estimates.

5.7. M_{tot}–Y_X

The $Y_{\rm X}$ parameter (Kravtsov et al. 2006), a measure of the total thermal energy in the ICM, is also a low scatter mass proxy (see Figure 6). As for the other scaling relations, we observe quite good agreement in the slope derived from independent studies and an offset in the normalization, in particular in the best fit derived by EB19 and AM13 (∼8% lower normalization). The offset is smaller, on the order of ∼5%, with respect to LL15 and AV09, while it is in perfect agreement with the result by Arnaud et al. (2010, hereafter MA10). If the offset is caused by the lower $M_{\rm gas}$ in low-mass systems, then we should observe a lower $M_{\rm tot}$–$Y_{\rm X}$ relation also for LL15 that includes systems with total masses down to $\sim 2 \times 10^{13}\,M_{\odot}$. Instead, the relation by LL15 has a lower normalization than the one from EB19, in particular in the low-mass regime. Unlike the other studies plotted in Figure 6, EB19 uses SZ-derived masses, which may suggest a mass trend of the SZ signal with the total mass that would result in an offset in the X-ray observables and total mass relations.

Almost all the studies find a slope of the $M_{\rm tot}$–$Y_{\rm X}$ relation shallower than what is expected from the self-similar scenario (i.e., $\beta = 0.6$). This may be caused by the increasing gas fractions for increasing total cluster masses. In fact, LL15 found that the slopes of the $M_{\rm tot}$–$Y_{\rm X}$ relation, derived in the low- and high-mass regimes, agree well with the prediction of the self-similar scenario. However, the normalizations are quite different, with the galaxy groups having a >10% higher normalization than the clusters, due to their average lower gas fraction. This offset in the normalization leads to a slightly shallower relation, when fitting all the systems together.

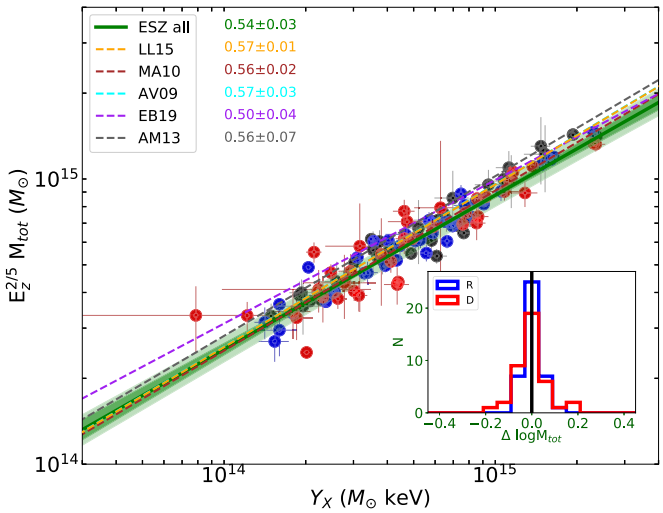

Figure 6. $M_{\rm tot}$–$Y_{\rm X}$ relation for the ESZ clusters investigated in this work. The most relaxed and most disturbed clusters are shown in blue and red, respectively. The green line represents the fitted relation with γ free to vary. The dark and light shaded areas represent the 1σ statistical error and scatter, respectively. In the inset plot, we show the histogram of the log space residuals from the fitted $M_{\rm tot}$–$Y_{\rm X}$ relation. As for the $M_{\rm tot}$–$M_{\rm gas}$ relation, there is good agreement between the slopes obtained from the different samples but an offset in the normalization. This, together with the good agreement between the relations obtained with the subsamples of relaxed and disturbed ESZ clusters, suggests that the $M_{\rm tot}$–$Y_{\rm X}$ relation is insensitive to the dynamical state of the objects but dependent on the mass range investigated. The effect is smaller than that observed for the $M_{\rm tot}$–$M_{\rm gas}$ relation. The acronyms in the legend are described in Sections 5.1, 5.4, 5.6, and 5.7.

The relations, determined for relaxed and disturbed clusters separately, are in good agreement. Thus, as for the $M_{\rm tot}$–$M_{\rm gas}$ relation, the $M_{\rm tot}$–$Y_{\rm X}$ slope is insensitive to the dynamical state of the objects, but it may still have a small dependence on the mass range considered, which affects the normalization, although with a lower impact than what is seen in the $M_{\rm tot}$–$M_{\rm gas}$ relation. As for the $M_{\rm tot}$–$M_{\rm gas}$ relation, there is a hint of a smaller scatter for relaxed clusters, but the difference is within the statistical uncertainties. Using the core-excised temperatures to calculate the $Y_{\rm X}$ parameters does not impact either the shape or the scatter of the relations. This confirms that the relation is basically insensitive to the influence of AGN feedback and/or star formation, as suggested by the numerical simulations (e.g., Kravtsov et al. 2006; Nagai et al. 2007). The similarity in the scatter of the $M_{\rm tot}$–$M_{\rm gas}$ and $M_{\rm tot}$–$Y_{\rm X}$ for both relaxed and disturbed systems suggests that the scatter in the two relations is probably driven by the same processes.

5.8. M_{tot}–T_{exc}

In Figure 7 we compare our $M_{\rm tot}$–$T_{\rm exc}$ relation with the relations available in the literature by LL15, AV09, AM10, XXL, EB19,

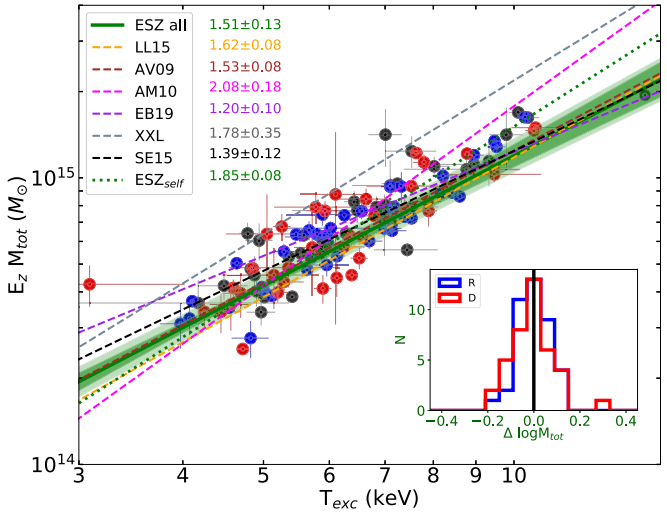

Figure 7. $M_{\rm tot}$–$T_{\rm exc}$ relation for the ESZ clusters investigated in this work. The most relaxed and most disturbed clusters are shown in blue and red, respectively. Clusters that are not in these two subsamples are shown in black. The green line represents the fitted relation with the redshift evolution free to vary. The dark and light shaded areas represent the 1σ statistical error and scatter, respectively. In the inset plot we show the histogram of the log space residuals from the fitted $M_{\rm tot}$–$T_{\rm exc}$ relation. The acronyms in the legend are described in Sections 5.1, 5.4, and 5.6.

and SE15. The slope for the ESZ sample, $\beta = 1.508 \pm 0.126$, is in agreement with the self-similar expectations (i.e., $\beta = 1.5$), but with a positive redshift evolution at the $\sim 3\sigma$ level. However, if the redshift evolution is forced to be self-similar, the fit prefers a much steeper relation (i.e., $\beta = 1.823 \pm 0.076$), which is in better agreement with the result by AM10, who fitted jointly the luminosity, temperature, and total cluster mass, accounting for the selection biases, and assuming a self-similar redshift evolution. The $M_{\rm tot}$–T relation determined with core-excised temperatures is not significantly different from that obtained using the core-included temperatures. Relaxed and disturbed clusters share a similar relation, and also the scatter is not significantly different ($\sigma_{Y|Z} = 0.037 \pm 0.015$ vs. $\sigma_{Y|Z} = 0.046 \pm 0.022$ for the relaxed and unrelaxed subsamples, respectively), as instead was observed by Lieu et al. (2016) for the XXL sample using WL masses and *XMM-Newton* temperatures within a 300 kpc radius. A similar level of the scatter for the temperature suggests that the processes that alter the homogeneous temperature distribution have a relatively small impact on the scatter of the scaling relations.

6. Discussion

All the observed scaling relations, with the exception of the $M_{\rm tot}$–$T_{\rm exc}$, have a slope that deviates from the expectation of the self-similar scenario by more than 2σ (see Figure 8, left panel) but are statistically consistent with the results from the literature (within 1σ if the same fitting method is used). There are also hints that relaxed systems have steeper relations than disturbed clusters (see Table 2), again with the exception of the $M_{\rm tot}$–$T_{\rm exc}$ relation, but that needs to be confirmed with a larger sample to strongly reduce the statistical uncertainties of the fits.

In the case of the L–$M_{\rm tot}$ relations, we observe quite large normalization offsets between the different studies. This is partially associated with the assumed fitting procedure and the choice of keeping the redshift evolution frozen or free (see Appendix B for more details). Strongly contributing to the offset is also the different fractions of relaxed and disturbed systems in the investigated samples. In fact, on average, relaxed systems have a 30% higher X-ray soft-band (0.1–2.4 keV) luminosity than disturbed clusters for the same mass. The origin of this difference is the lack of self-similarity in the gas density profiles of relaxed and disturbed clusters as discussed by Maughan et al. (2012). Disturbed clusters have flatter profiles, while relaxed clusters have more centrally concentrated gas density profiles. Moreover, Maughan et al. (2012) found a temperature dependence for the profiles of the disturbed systems with hotter clusters having higher densities than the cooler clusters. They did not find the same dependence for the relaxed clusters (see also Mantz et al. 2016). The ESZ sample has a similar behavior, and we also find a temperature dependence for relaxed clusters in the low-redshift ($z < 0.2$) regime, while the most distant and relaxed clusters of our sample show similar profiles, independent of their temperature. These results complicate the comparison of the L–$M_{\rm tot}$ relation from different works. To illustrate why, we compare the average profile of the ESZ sample with the REXCESS sample (see left panel of Figure 9). The two samples have a similar electron density in the center, but in the outer regions, the ESZ clusters show a much higher density than the REXCESS clusters. Since the two samples span a different mass range, in the middle panel of Figure 9 we only compare the massive systems, which show much better agreement in the outer regions, while showing a higher gas density in the core of the REXCESS clusters. However, since ESZ clusters are on average more disturbed than REXCESS clusters (e.g., Lovisari et al. 2017), in the right panel of Figure 9 we compare only the most relaxed systems in ESZ with all REXCESS clusters and find that the agreement is very good. This agreement reflects the good match between the relation found by GP09 and that from the most relaxed objects in the ESZ sample. However, the different shape of the electron density profiles for relaxed and disturbed systems, together with their temperature/redshift dependence and the relative fraction of relaxed/disturbed systems in the samples, has an impact on the observed slopes and normalizations and also on the cluster redshift evolution.

To further complicate the comparison, we note that different studies compute the total masses in different ways, which can easily result in an offset of 10%–20% (e.g., Sereno & Ettori 2015a; Pratt et al. 2019). The assumption of $N_{\rm H}$ (LAB vs. TOT), plasma model (e.g., mekal vs. apec v1.3.1 vs. apec v3.0.9), and abundance tables (e.g., ASPL from Asplund et al. 2009 vs. ANGR from Anders & Grevesse 1989) in the spectral fitting and in the conversion of the total count rates from the SB to the cluster fluxes also can cause an offset in the y-direction (i.e., in X-ray luminosity). Moreover, some relations have been obtained using the luminosities derived with RASS data, while others use the higher-quality data of *Chandra* and *XMM-Newton*, which allow a more accurate point-source detection. Similar arguments can be applied to the L–T relation, with the complication that temperatures obtained with different detectors can vary significantly, with a larger deviation observed for hot clusters, which therefore can also lead to a different slope. Interestingly, both the L–T and L–$M_{\rm tot}$ relations from different studies tend to converge, when the core-excised luminosities are used, which points to the different fraction of relaxed and disturbed systems as the main contribution for the observed offset.

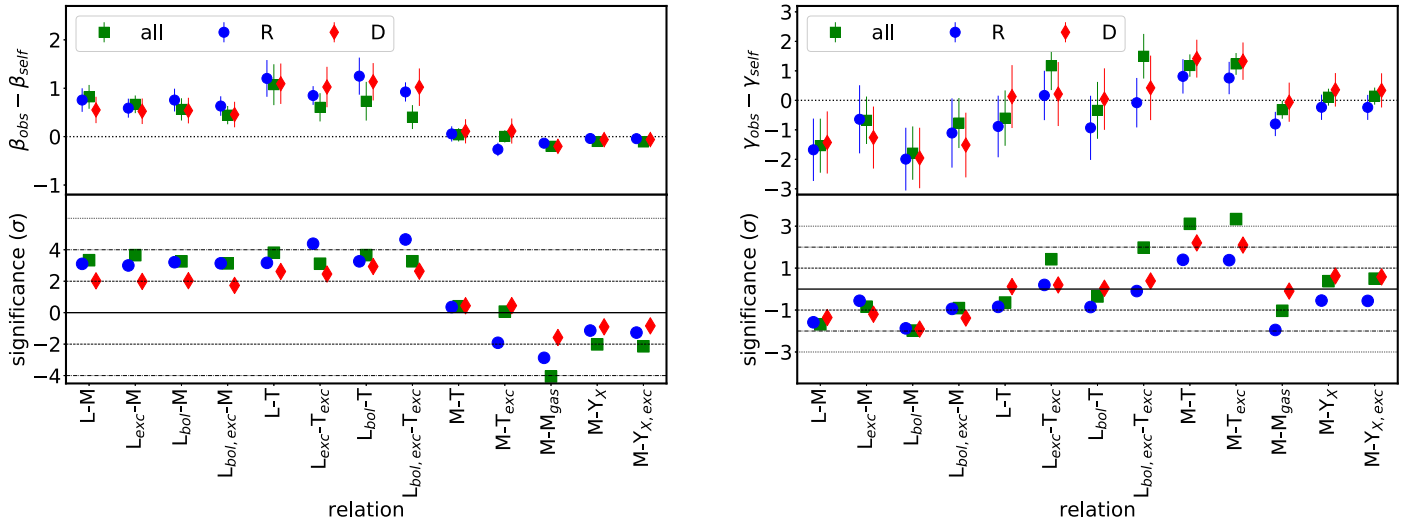

Figure 8. Overview of the fitted slopes β (left panel) and redshift evolution factors γ (right panel) with respect to the self-similar predictions (see Table 1). The results for the full sample are shown with green squares, while the results for the subsamples of relaxed (R) and disturbed (D) clusters are shown with blue circles and red diamonds, respectively. In the top panels, we show the difference between the observed and predicted values (i.e., if a relation behaves self-similarly, the data point would be consistent with zero). In the bottom panels we show how significantly the parameters deviate from the prediction.

The relatively good agreement between the $L_{X,exc}$–T_{exc} relation of AM10 with the other relations may also indicate that their flatter slope for the $L_{X,exc}$–M_{tot} relation is probably related to a mass-dependent effect on the total mass estimation.

The M_{tot}–M_{gas} and M_{tot}–Y_X relations are in good agreement between the different studies, particularly if self-similar redshift evolution is assumed. One of the reasons is that, differently from the luminosity, M_{gas} depends linearly on the gas density, reducing the impact of different selection methods. This is probably also due to the smaller offset between the relation obtained with the relaxed and disturbed cluster subsamples (i.e., only $\leqslant$5% difference). Interestingly, both the ESZ and SPT samples suggest a slightly flatter M_{tot}–Y_X relation than the relations derived from X-ray-selected samples, although at low significance.

Special discussion is needed for the M_{tot}–T relation. As can be seen in Figure 7, there is some tension between the best-fit relations determined in different studies, in terms of both slope and normalization, with the latter easily connected to the method and/or proxy used for the total mass estimate. The slope can be as shallow as 1.25 ± 0.16, as found by EB19, or as steep as 2.08 ± 0.18, as found by AM10. The consistency of the M_{tot}–T relation for galaxy groups and clusters (e.g., Sun et al. 2009; Lovisari et al. 2015) excludes the possibility that the differences are related to the mass (temperature) range investigated. Moreover, the agreement of the M_{tot}–T relation at low- and high-mass ends suggests that nongravitational processes are not strongly impacting this relation. Therefore, the offset seen in Figure 7 may point to a possible bias introduced in the estimate of the total mass. For instance, EB19 used the SZ masses to derive the scaling relations, and if the SPT mass estimates suffer from a mass-dependent bias as found by the Planck mass estimates, it could explain the shallower relation.

All the fitted relations for the ESZ sample prefer different values of γ with respect to the expectations of the self-similar scenario. However, given the relatively low redshift (i.e., $z_{med} \approx 0.2$) of the sample, only the value of γ for the M_{tot}–T relation lies more than 2σ from the self-similar value (see Figure 8, right panel). The best fits for the L–M_{tot} and L–T relations suggest a negative evolution of the scaling laws, in agreement with the finding by Reichert et al. (2011), who combined several published data sets to investigate the evolution of the X-ray scaling relations to $z = 1.46$. The negative evolution estimated by Reichert et al. (2011) is more significant than the one estimated with the ESZ sample. This is likely due to the larger redshift range covered by their sample, but also because only X-ray-selected clusters were used. In fact, interestingly, for the ESZ sample we found a systematic trend to have a larger evolution for the most relaxed objects than for the most disturbed clusters. This indicates that relaxed and disturbed systems may evolve differently. We note that, given the large errors associated with γ, this result is not conclusive and a detailed investigation with a larger sample, which also includes more distant clusters, should be performed. Nonetheless, the effect of the cores in the L–M_{tot} and L–T relations should be taken into account, not only for the effect on the scatter but also for the impact on the normalization and on the redshift evolution.

For example, the offset between the ESZ and SPT L_X–M_{tot} relation decreases from $\sim$45% to $\sim$23% when self-similar redshift evolution (i.e., $\gamma = 2$) is assumed. If relaxed and disturbed clusters evolve differently, and since the fraction of relaxed and disturbed clusters in the ESZ and SPT samples could be different, then forcing the same evolution may reduce the offset. However, that would be an extra effect on top of the offset caused by the different fraction of relaxed/disturbed systems (i.e., the larger the fraction of relaxed objects in the sample, the higher is the normalization). Unfortunately, we do not know the dynamical state for the SPT clusters analyzed by EB19.

The evolution factor γ determined for the global and core-excised luminosity relations is consistent in the case of disturbed clusters, while it is different for relaxed clusters. In particular, using the core-excised luminosities leads to a γ value consistent with the one derived for disturbed clusters and in better agreement with the expectations from the self-similar scenario. This suggests either that the peaked and relaxed clusters evolve differently from the disturbed clusters or that the cool cores mimic the evolution.

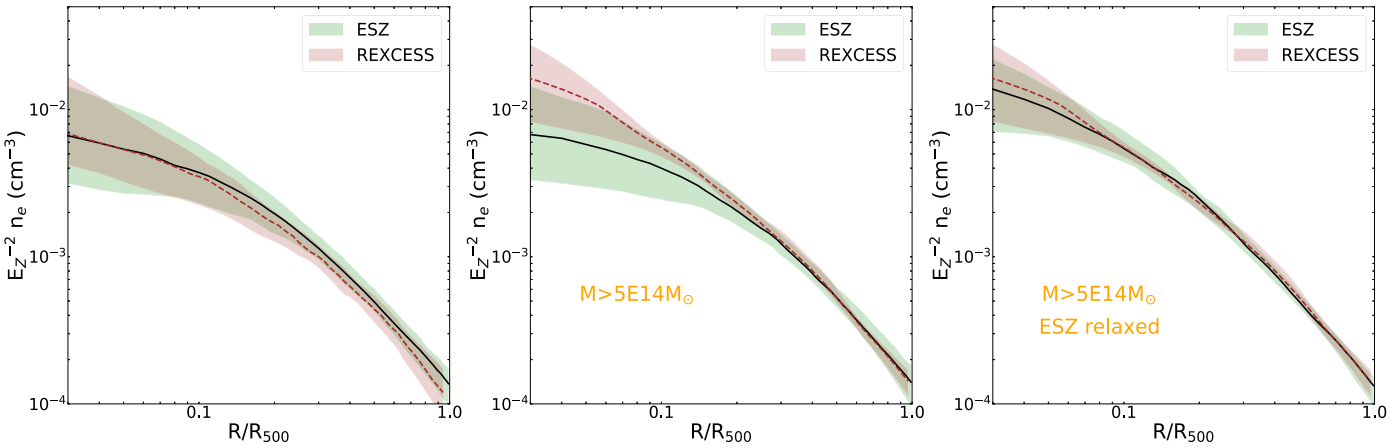

Figure 9. Left: comparison between the average density profiles for REXCESS and ESZ samples. Middle: as in the left panel, but using for both samples only clusters with a $M_{\rm tot} > 5 \times 10^{14}\,M_\odot$. Right: as in the middle panel, but using only the relaxed subsample for the ESZ clusters.

Given the higher normalization in the scaling relations of relaxed than disturbed systems, and since flux selected samples have been shown to have a larger fraction of relaxed clusters, the lower normalization found by GS17, AM10, and AM16 must have a different explanation. For example, in this paper we determined the masses as in GS17, but using *XMM-Newton*, which is known to deliver lower temperatures than *Chandra*. It is possible that in the high-mass regime the masses obtained by GS17 are higher than the ones derived in this work because of the higher temperatures determined with *Chandra*. However, since the temperatures at large radii drop to values where *Chandra* and *XMM-Newton* agree better, the difference may be smaller. Indeed, Martino et al. (2014) obtained consistent results for the total hydrostatic masses for the same clusters observed with both *Chandra*- and *XMM-Newton*-based measurements. Therefore, a more detailed investigation is required to understand this difference.

The relation determined for the most relaxed clusters in our sample agrees well with the relation determined by GP09 for the REXCESS sample, which is dominated by centrally peaked and relaxed systems. The significant overlap between the n_e profiles from the REXCESS sample and our subsample of relaxed systems fully explains this good agreement.

The $M_{\rm tot}$–T relation shows a positive evolution with respect to the self-similar prediction. The evolution is detected at more than the 3σ level (see Figure 8). The results by EB19 with the SPT clusters are also consistent with a positive evolution, although detected only at the 1σ level. Studies of X-ray-selected samples found seemingly contradictory results: e.g., Ettori et al. (2004) and Reichert et al. (2011) found no evolution, while Mantz et al. (2016) found a $\sim 2\sigma$ positive evolution. The fact that the positive evolution is observed more significantly with SZ-selected samples is probably associated with the larger fraction of disturbed clusters than in the X-ray-selected samples and a better sampling of the full halo population. Indeed, the redshift evolution for the subsample of relaxed clusters is closer to the prediction of the self-similar scenario. This finding is consistent with the picture that clusters at higher redshift are on average more disturbed (as confirmed by the mild correlation of the centroid-shift with the redshift); therefore, their temperatures are hotter than what one would expect from self-similar evolution. Moreover, disturbed clusters tend to have a larger hydrostatic bias, which could potentially mimic the evolution. Although observationally this

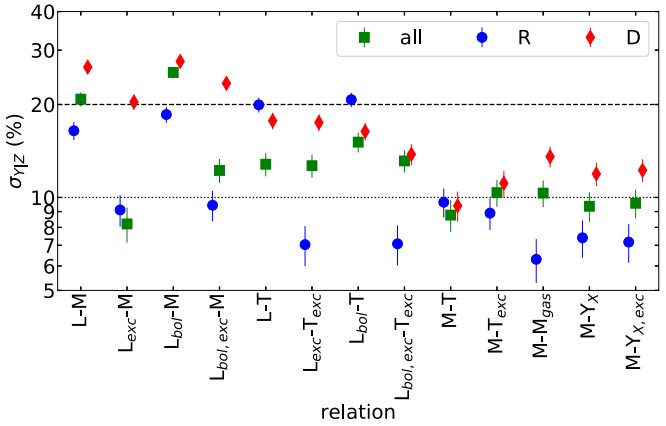

Figure 10. Overview of the intrinsic scatter, $\sigma_{Y|Z}$, expressed in percent. The results for the full sample are shown with green squares, while the results for the subsamples of relaxed (R) and disturbed (D) clusters are shown with blue circles and red diamonds, respectively.

is the first time that the evolution was detected so significantly, a positive evolution was predicted by recent simulations. For example, Le Brun et al. (2017) investigated a large population of groups and clusters obtained with the cosmo-OWLS suite in cosmological hydrodynamical simulations and found a positive evolution of the $M_{\rm tot}$–T relation, independent of the included ICM physics. More recently, Truong et al. (2018) also found that the normalization of the $M_{\rm tot}$–T relation varies only by $\sim$20% between $z = 0.6$ and $z = 0$ (roughly the same redshift range investigated in our paper) instead of the $\sim$40% predicted by the self-similar scenario. The evolution is somehow stronger when AGN feedback is included in the simulations. The reason for this good agreement between observations and simulations may be due to the characteristic SZ cluster selection, which is approximately a mass selection. This is more representative of the cluster selection sampled by hydrodynamical simulations.

The scatter in the scaling relations is the sum of different processes acting in different directions. In our study, apart from the $L_{\rm X}$–T, $L_{\rm bol}$–T, and $M_{\rm tot}$–T relations, the subsample of relaxed clusters shows a lower scatter than the subsample of disturbed clusters (see Figure 10). Moreover, the scatter is clearly reduced by excluding the core regions to compute both luminosity and temperature, although the use of the core-excised temperatures has a much lower contribution in the scatter reduction than the core-excised luminosities. This

suggests that temperature inhomogeneities do not play a major role in the scatter of the scaling relations. As found in previous studies and by numerical simulations (e.g., Le Brun et al. 2017), we found that the $M_{\rm tot}$–$M_{\rm gas}$, $M_{\rm tot}$–T, and $M_{\rm tot}$–$Y_{\rm X}$ relations all have relatively low scatter. Moreover, the intrinsic scatter of the relations is further reduced, if only the relaxed clusters are considered.

Depending on the orientation of the cluster, the estimated $M_{\rm gas}$ can be easily incorrect (i.e., typically the $M_{\rm gas}$ is overestimated if the cluster is elongated along the line of sight, while it is underestimated if the cluster is elongated in the plane of the sky; see Piffaretti et al. 2003 for more details). Since the temperature structures have a small effect on the scatter, the determination of $M_{\rm gas}$ by ignoring triaxiality, substructures, and clumps could be one of the major drivers for the scatter in these relations.

7. Summary and Conclusion

We used archival *XMM-Newton* observations to determine the X-ray properties (i.e., $M_{\rm tot}$, $M_{\rm gas}$, kT, $L_{\rm X}$, $L_{\rm bol}$, $Y_{\rm X}$) of a representative sample of 120 Planck ESZ clusters to investigate the most common X-ray scaling relations: L–$M_{\rm tot}$, L–T, $M_{\rm tot}$–$M_{\rm gas}$, $M_{\rm tot}$–$Y_{\rm X}$, and $M_{\rm tot}$–T. We fit these relations, leaving free to vary the slope, normalization, redshift evolution, and intrinsic scatter in both X and Y variables. Our results are the following:

1. The slopes of the scaling relations derived with SZ-selected samples are in relatively good agreement with the relations derived from X-ray-selected samples, particularly when the same fitting procedure is used. However, for most of the relations, there is some tension in the normalizations that can only partially be ascribed to the fitting algorithm. Most differences come from the different fraction of relaxed and disturbed systems in the samples, which strongly depends on the different selection functions (e.g., SZ vs. X-ray). On top of that, differences also arise from different methods used to determine the global cluster properties (e.g., different mass proxies for the total mass) and the use of different instruments (e.g., gas temperatures from *Chandra* instead of *XMM-Newton*). Moreover, because of the mass dependence of the gas fraction, the range of masses considered in each sample has an impact on the slope, the normalization, and probably also the evolution of the different relations.
2. There is a hint for a different redshift evolution in relaxed and disturbed clusters. When the core regions are removed, the γ values determined for the two subsamples tend to be in better agreement and also in better agreement with the self-similar predictions.
3. The positive redshift evolution of the $M_{\rm tot}$–T relation suggests an evolution of the kinetic-to-thermal energy ratio of the ICM in clusters. Higher-redshift clusters are on average more disturbed, so that the contribution to the nonthermal pressure by large-scale motions is larger. The γ value obtained for relaxed clusters is in better agreement with the self-similar prediction than the one obtained for the most disturbed systems, in support of this scenario.
4. The $M_{\rm tot}$–$M_{\rm gas}$ and in particular the $M_{\rm tot}$–$Y_{\rm X}$ relations show the weakest dependence on the dynamical state of the systems, as suggested by numerical simulations. Both relations show consistent slopes (although shallower than the self-similar predictions) and normalizations. Moreover, they also show a redshift evolution in relatively good agreement with the self-similar expectations.
5. The intrinsic scatter of the relations derived for the relaxed cluster subsample is smaller than the one derived for the disturbed subsample. Moreover, removing the central regions of the clusters further reduces the scatter, particularly for the most relaxed systems.

The paper is based on observations obtained with *XMM-Newton*, an ESA science mission with instruments and contributions directly funded by ESA Member States and NASA. We thank the anonymous referee for his/her review of the manuscript. We also acknowledge useful discussions with M. Arnaud. L.L. acknowledges support from NASA through contracts 80NSSCK0582 and 80NSSC19K0116. W.R.F. and C.J. acknowledge support from the Smithsonian Institution and the High Resolution Camera Project through NASA contract NAS8-03060. G.S. acknowledges support from NASA through contracts AR9-20013X. S.E. and M.S. acknowledge financial contribution from the contracts ASI 2015-046-R.0 and ASI-INAF n.2017-14-H.0 and from INAF "Call per interventi aggiuntivi a sostegno della ricerca di main stream di INAF." G. W.P. acknowledges funding from the European Research Council under the European Union's Seventh Framework Programme (FP7/2007-2013)/ERC grant agreement No. 340519 and from the French space agency CNES.

Facility: XMM-Newton.

Software: XSPEC (Arnaud 1996), SAS (v16.0.0; Gabriel et al. 2004).

Appendix A
Cluster Properties

All the X-ray properties used in this paper and calculated within R_{500} are listed in Table 3.

Appendix B
Comparisons between Different Fitting Methods

In this paper we compared our results with the best-fit relations from papers that used different linear regression techniques for their analysis. This complicates the comparison and the interpretation of the different results because they are affected by how one treats the measurement errors, which may be heteroscedastic and correlated, and the intrinsic scatter. On top of that, the treatment of the selection effects that bias some cluster samples also has a nonnegligible effect on the regression results. Many methods have been proposed to account for these effects (see, e.g., Kelly 2007; Mantz 2016; Sereno 2016, and references therein), each with their advantages and disadvantages. Here we compare the results from LIRA (Sereno 2016), the technique used in this paper, with BCES (Akritas & Bershady 1996) and MLINMIX (Kelly 2007), two linear regression techniques, publicly available, and widely used when fitting scaling relations. We summarize the results in Table 4, and we plot the $L_{\rm X}$–$M_{\rm tot}$ and $L_{\rm X}$–T relations for illustration in Figure 11. For both relations, the slope obtained with LIRA leaving all the parameters free to vary (in green) is the steepest and is in fairly good agreement with the result of the orthogonal method with BCES (in black). However, in the latter case the redshift evolution is forced to be self-similar in contrast to the negative redshift evolution

Table 3
Cluster Properties

Planck Name	z	$M_{\rm tot}$ ($10^{14}\,M_\odot$)	$M_{\rm gas}$ ($10^{13}\,M_\odot$)	kT (keV)	$kT_{\rm exc}$ (keV)	$L_{\rm X}$ (erg s^{-1})	$L_{\rm X,exc}$ (erg s^{-1})	$L_{\rm bol}$ (erg s^{-1})	$L_{\rm bol,exc}$ (erg s^{-1})	N_T	f_T	$N_{\rm sb}$	$f_{\rm sb}$
G000.44–41.83	0.165	$5.01^{+0.55}_{-0.48}$	$6.61^{+0.36}_{-0.33}$	$5.85^{+0.32}_{-0.32}$	$5.82^{+0.43}_{-0.43}$	$3.79^{+0.25}_{-0.25}$	$2.88^{+0.13}_{-0.13}$	$8.36^{+0.78}_{-0.78}$	$6.36^{+0.47}_{-0.47}$	6	1.00	20	1.21
G002.74–56.18	0.141	$4.96^{+0.43}_{-0.28}$	$5.63^{+0.21}_{-0.14}$	$5.36^{+0.12}_{-0.12}$	$5.39^{+0.18}_{-0.18}$	$4.47^{+0.16}_{-0.16}$	$2.71^{+0.07}_{-0.07}$	$9.96^{+0.49}_{-0.49}$	$6.03^{+0.23}_{-0.23}$	10	0.94	49	1.08
G003.90–59.41	0.151	$6.94^{+0.19}_{-0.19}$	$8.65^{+0.08}_{-0.08}$	$7.06^{+0.13}_{-0.13}$	$6.46^{+0.14}_{-0.14}$	$7.13^{+0.24}_{-0.24}$	$4.61^{+0.17}_{-0.17}$	$18.06^{+0.67}_{-0.67}$	$11.62^{+0.43}_{-0.43}$	10	0.98	63	1.08
G006.70–35.54	0.089	$2.42^{+0.04}_{-0.03}$	$4.27^{+0.05}_{-0.08}$	$4.72^{+0.08}_{-0.08}$	$4.62^{+0.09}_{-0.09}$	$2.44^{+0.09}_{-0.09}$	$2.08^{+0.08}_{-0.08}$	$4.67^{+0.25}_{-0.25}$	$3.98^{+0.21}_{-0.21}$	15	1.14	45	1.18
G006.78+30.46	0.203	$17.56^{+0.28}_{-0.27}$	$32.00^{+0.24}_{-0.22}$	$14.37^{+0.12}_{-0.12}$	$15.01^{+0.16}_{-0.16}$	$23.84^{+0.36}_{-0.36}$	$16.55^{+0.13}_{-0.13}$	$86.79^{+1.74}_{-1.74}$	$60.27^{+0.84}_{-0.84}$	19	1.26	171	1.62
G008.44–56.35	0.149	$3.61^{+0.08}_{-0.07}$	$4.64^{+0.05}_{-0.04}$	$5.12^{+0.08}_{-0.08}$	$4.91^{+0.10}_{-0.10}$	$3.47^{+0.12}_{-0.12}$	$2.31^{+0.08}_{-0.08}$	$6.78^{+0.34}_{-0.34}$	$4.54^{+0.22}_{-0.22}$	8	1.10	41	1.24
G008.93–81.23	0.307	$10.39^{+0.24}_{-0.23}$	$15.64^{+0.13}_{-0.13}$	$8.78^{+0.09}_{-0.09}$	$8.43^{+0.10}_{-0.10}$	$13.12^{+0.31}_{-0.31}$	$9.72^{+0.17}_{-0.17}$	$36.54^{+1.21}_{-1.21}$	$27.09^{+0.70}_{-0.70}$	8	0.97	78	1.03
G021.09+33.25	0.151	$6.88^{+0.20}_{-0.18}$	$10.45^{+0.32}_{-0.35}$	$6.25^{+0.14}_{-0.14}$	$8.77^{+0.31}_{-0.31}$	$16.07^{+0.18}_{-0.18}$	$6.84^{+0.10}_{-0.10}$	$38.83^{+0.55}_{-0.55}$	$16.51^{+0.25}_{-0.25}$	10	1.21	86	1.24
G036.72+14.92*	0.152	$5.21^{+0.32}_{-0.29}$	$8.16^{+0.29}_{-0.28}$	$7.44^{+0.66}_{-0.66}$	$6.89^{+1.02}_{-1.02}$	$5.97^{+0.27}_{-0.27}$	$4.00^{+0.17}_{-0.17}$	$15.59^{+1.11}_{-1.11}$	$10.43^{+0.71}_{-0.71}$	3	0.51	9	0.87
G039.85–39.98	0.176	$3.77^{+0.47}_{-0.17}$	$5.32^{+0.36}_{-0.17}$	$5.89^{+0.14}_{-0.14}$	$5.82^{+0.16}_{-0.16}$	$2.91^{+0.12}_{-0.12}$	$2.02^{+0.10}_{-0.10}$	$6.54^{+0.32}_{-0.32}$	$5.69^{+0.28}_{-0.28}$	7	1.22	71	1.43
G042.82+56.61	0.072	$4.65^{+0.15}_{-0.13}$	$6.01^{+0.08}_{-0.07}$	$4.83^{+0.07}_{-0.07}$	$4.79^{+0.09}_{-0.09}$	$3.18^{+0.08}_{-0.08}$	$2.24^{+0.05}_{-0.05}$	$6.74^{+0.22}_{-0.22}$	$4.74^{+0.14}_{-0.14}$	15	0.74	42	0.88
G046.08+27.18	0.389	$6.26^{+0.61}_{-0.48}$	$9.90^{+0.35}_{-0.30}$	$5.93^{+0.30}_{-0.30}$	$5.65^{+0.29}_{-0.29}$	$7.51^{+0.41}_{-0.41}$	$6.26^{+0.28}_{-0.28}$	$17.12^{+1.47}_{-1.47}$	$14.28^{+1.10}_{-1.10}$	3	1.08	15	1.17
G046.50–49.43	0.085	$6.05^{+0.28}_{-0.26}$	$6.24^{+0.09}_{-0.08}$	$5.59^{+0.12}_{-0.12}$	$5.21^{+0.14}_{-0.14}$	$3.34^{+0.12}_{-0.12}$	$2.28^{+0.07}_{-0.07}$	$7.95^{+0.39}_{-0.39}$	$5.43^{+0.23}_{-0.23}$	15	0.67	58	0.75
G049.20+30.86	0.164	$5.86^{+0.16}_{-0.16}$	$6.51^{+0.07}_{-0.07}$	$5.47^{+0.08}_{-0.08}$	$6.28^{+0.17}_{-0.17}$	$8.70^{+0.18}_{-0.18}$	$3.83^{+0.06}_{-0.06}$	$22.46^{+0.74}_{-0.74}$	$9.89^{+0.29}_{-0.29}$	8	0.99	24	0.99
G049.33+44.38	0.097	$3.84^{+0.46}_{-0.38}$	$3.85^{+0.18}_{-0.17}$	$4.90^{+0.17}_{-0.17}$	$4.80^{+0.23}_{-0.23}$	$1.68^{+0.08}_{-0.08}$	$1.22^{+0.04}_{-0.04}$	$3.60^{+0.23}_{-0.23}$	$2.63^{+0.13}_{-0.13}$	8	0.61	26	0.82
G049.66–49.50	0.098	$4.81^{+0.21}_{-0.19}$	$4.41^{+0.08}_{-0.08}$	$4.64^{+0.08}_{-0.08}$	$4.81^{+0.14}_{-0.14}$	$3.44^{+0.12}_{-0.12}$	$1.74^{+0.05}_{-0.05}$	$7.26^{+0.33}_{-0.33}$	$3.67^{+0.15}_{-0.15}$	10	0.68	36	0.68
G053.52+59.54	0.113	$5.87^{+0.20}_{-0.15}$	$7.03^{+0.10}_{-0.08}$	$6.58^{+0.14}_{-0.14}$	$6.31^{+0.16}_{-0.16}$	$4.08^{+0.11}_{-0.11}$	$3.08^{+0.04}_{-0.04}$	$9.74^{+0.40}_{-0.40}$	$7.33^{+0.20}_{-0.20}$	5	0.81	38	0.96
G055.60+31.86	0.224	$6.54^{+0.18}_{-0.15}$	$9.41^{+0.12}_{-0.10}$	$7.39^{+0.11}_{-0.11}$	$7.30^{+0.14}_{-0.14}$	$10.06^{+0.30}_{-0.30}$	$5.34^{+0.21}_{-0.21}$	$25.87^{+0.85}_{-0.85}$	$13.65^{+0.56}_{-0.56}$	9	1.03	53	1.10
G055.97–34.88	0.124	$5.41^{+0.45}_{-0.37}$	$3.44^{+0.09}_{-0.09}$	$6.25^{+0.37}_{-0.37}$	$5.50^{+0.37}_{-0.37}$	$2.11^{+0.08}_{-0.08}$	$1.54^{+0.07}_{-0.07}$	$5.47^{+0.32}_{-0.32}$	$4.01^{+0.22}_{-0.22}$	7	0.42	18	0.51
G056.81+36.31	0.095	$3.98^{+0.08}_{-0.07}$	$5.12^{+0.04}_{-0.04}$	$4.98^{+0.05}_{-0.05}$	$4.83^{+0.07}_{-0.07}$	$4.34^{+0.12}_{-0.12}$	$2.35^{+0.06}_{-0.06}$	$9.30^{+0.31}_{-0.31}$	$5.05^{+0.17}_{-0.17}$	15	1.01	99	1.10
G056.96–55.07	0.447	$9.62^{+0.25}_{-0.25}$	$15.23^{+0.14}_{-0.14}$	$7.63^{+0.12}_{-0.12}$	$7.58^{+0.13}_{-0.13}$	$14.61^{+0.39}_{-0.39}$	$11.98^{+0.30}_{-0.30}$	$38.36^{+1.50}_{-1.50}$	$31.48^{+1.16}_{-1.16}$	5	0.91	48	0.94
G057.26–45.35	0.397	$13.17^{+0.64}_{-0.65}$	$18.61^{+0.29}_{-0.28}$	$10.39^{+0.33}_{-0.33}$	$9.99^{+0.44}_{-0.44}$	$25.32^{+0.73}_{-0.73}$	$12.75^{+0.27}_{-0.27}$	$82.81^{+4.14}_{-4.14}$	$41.70^{+1.75}_{-1.75}$	5	0.91	32	1.00
G058.28+18.59	0.065	$3.72^{+0.06}_{-0.07}$	$4.54^{+0.20}_{-0.05}$	$5.01^{+0.04}_{-0.04}$	$4.87^{+0.05}_{-0.05}$	$2.01^{+0.04}_{-0.04}$	$1.66^{+0.02}_{-0.02}$	$4.03^{+0.11}_{-0.11}$	$3.31^{+0.08}_{-0.08}$	19	1.01	65	1.07
G062.42–46.41	0.091	$3.26^{+0.39}_{-0.15}$	$2.87^{+0.13}_{-0.12}$	$4.25^{+0.08}_{-0.08}$	$4.28^{+0.12}_{-0.12}$	$1.42^{+0.05}_{-0.05}$	$1.15^{+0.04}_{-0.04}$	$2.65^{+0.13}_{-0.13}$	$2.14^{+0.10}_{-0.10}$	8	0.41	30	0.56
G067.23+67.46	0.171	$8.11^{+0.17}_{-0.18}$	$10.44^{+0.08}_{-0.12}$	$8.16^{+0.13}_{-0.13}$	$7.65^{+0.17}_{-0.17}$	$10.96^{+0.16}_{-0.16}$	$6.90^{+0.27}_{-0.27}$	$30.38^{+0.63}_{-0.63}$	$19.11^{+0.55}_{-0.55}$	14	1.03	71	1.08
G071.61+29.79	0.157	$4.24^{+0.76}_{-0.59}$	$5.32^{+0.51}_{-0.43}$	$4.88^{+0.36}_{-0.36}$	$4.93^{+0.42}_{-0.42}$	$2.44^{+0.15}_{-0.15}$	$2.20^{+0.12}_{-0.12}$	$4.58^{+0.39}_{-0.39}$	$4.13^{+0.32}_{-0.32}$	4	0.95	15	1.05
G072.63+41.46	0.228	$10.71^{+0.42}_{-0.39}$	$16.51^{+0.26}_{-0.25}$	$8.95^{+0.25}_{-0.25}$	$8.91^{+0.30}_{-0.30}$	$14.61^{+0.50}_{-0.50}$	$10.44^{+0.29}_{-0.29}$	$45.16^{+2.48}_{-2.48}$	$32.30^{+1.58}_{-1.58}$	9	0.97	45	0.97
G072.80–18.72	0.143	$5.33^{+0.17}_{-0.12}$	$8.25^{+0.11}_{-0.08}$	$5.93^{+0.09}_{-0.09}$	$5.99^{+0.12}_{-0.12}$	$5.69^{+0.19}_{-0.19}$	$3.99^{+0.13}_{-0.13}$	$13.32^{+0.59}_{-0.59}$	$9.35^{+0.38}_{-0.38}$	12	0.93	45	0.93
G073.96–27.82	0.233	$11.41^{+0.45}_{-0.38}$	$17.19^{+0.28}_{-0.24}$	$9.53^{+0.24}_{-0.24}$	$10.67^{+0.47}_{-0.47}$	$16.85^{+0.36}_{-0.36}$	$10.00^{+0.20}_{-0.20}$	$55.79^{+1.80}_{-1.80}$	$33.26^{+0.90}_{-0.90}$	9	0.94	17	1.01
G080.38–33.20	0.107	$3.66^{+0.07}_{-0.06}$	$3.83^{+0.03}_{-0.03}$	$5.41^{+0.07}_{-0.07}$	$4.82^{+0.08}_{-0.08}$	$2.19^{+0.04}_{-0.04}$	$1.46^{+0.02}_{-0.02}$	$4.87^{+0.12}_{-0.12}$	$3.26^{+0.06}_{-0.06}$	12	0.97	99	1.15
G080.99–50.90	0.300	$6.62^{+0.32}_{-0.23}$	$9.55^{+0.20}_{-0.17}$	$7.15^{+0.25}_{-0.25}$	$6.92^{+0.24}_{-0.24}$	$8.49^{+0.42}_{-0.42}$	$5.55^{+0.19}_{-0.19}$	$23.28^{+1.60}_{-1.60}$	$15.18^{+0.62}_{-0.62}$	6	0.94	20	1.19
G083.28–31.03	0.412	$7.68^{+0.47}_{-0.38}$	$12.48^{+0.30}_{-0.25}$	$7.24^{+0.31}_{-0.31}$	$7.02^{+0.34}_{-0.34}$	$11.78^{+0.40}_{-0.40}$	$8.31^{+0.17}_{-0.17}$	$30.61^{+1.90}_{-1.90}$	$21.26^{+0.83}_{-0.83}$	6	1.17	19	1.50
G085.99+26.71	0.179	$3.31^{+0.68}_{-0.57}$	$3.97^{+0.47}_{-0.41}$	$4.57^{+0.26}_{-0.26}$	$4.51^{+0.29}_{-0.29}$	$1.82^{+0.14}_{-0.14}$	$1.63^{+0.12}_{-0.12}$	$3.69^{+0.41}_{-0.41}$	$3.31^{+0.35}_{-0.35}$	4	0.66	13	1.18
G086.45+15.29*	0.260	$5.74^{+0.33}_{-0.25}$	$9.30^{+0.21}_{-0.18}$	$7.14^{+0.29}_{-0.29}$	$6.82^{+0.38}_{-0.38}$	$11.38^{+0.41}_{-0.41}$	$6.45^{+0.10}_{-0.10}$	$27.51^{+1.40}_{-1.40}$	$17.61^{+0.42}_{-0.42}$	7	1.10	22	1.16
G092.73+73.46	0.228	$6.18^{+0.32}_{-0.28}$	$10.72^{+0.29}_{-0.26}$	$7.13^{+0.19}_{-0.19}$	$7.09^{+0.21}_{-0.21}$	$7.74^{+0.31}_{-0.31}$	$5.72^{+0.15}_{-0.15}$	$19.00^{+1.08}_{-1.08}$	$10.90^{+0.41}_{-0.41}$	9	1.17	27	1.26
G093.91+34.90	0.081	$4.68^{+0.71}_{-0.50}$	$5.49^{+0.44}_{-0.33}$	$5.36^{+0.81}_{-0.81}$	$5.31^{+0.21}_{-0.21}$	$3.43^{+0.24}_{-0.24}$	$2.86^{+0.19}_{-0.19}$	$7.57^{+0.66}_{-0.66}$	$5.46^{+0.36}_{-0.36}$	7	0.85	44	1.07
G096.87+24.21	0.300	$5.47^{+2.40}_{-1.39}$	$6.28^{+1.08}_{-0.89}$	$5.05^{+0.54}_{-0.54}$	$4.99^{+0.60}_{-0.60}$	$3.04^{+0.32}_{-0.32}$	$2.65^{+0.23}_{-0.23}$	$6.80^{+0.97}_{-0.97}$	$5.94^{+0.74}_{-0.74}$	2	0.63	17	0.95
G097.73+38.11	0.171	$4.21^{+0.21}_{-0.20}$	$6.87^{+0.17}_{-0.16}$	$6.38^{+0.11}_{-0.11}$	$6.07^{+0.14}_{-0.14}$	$5.24^{+0.13}_{-0.13}$	$3.77^{+0.05}_{-0.05}$	$12.26^{+0.43}_{-0.43}$	$8.84^{+0.19}_{-0.19}$	9	1.00	18	1.07
G098.95+24.86	0.093	$3.25^{+0.35}_{-0.15}$	$2.99^{+0.14}_{-0.07}$	$4.97^{+0.20}_{-0.20}$	$4.94^{+0.28}_{-0.28}$	$1.28^{+0.06}_{-0.06}$	$0.86^{+0.03}_{-0.03}$	$2.77^{+0.19}_{-0.19}$	$1.87^{+0.11}_{-0.11}$	8	0.72	22	0.74
G106.73–83.22	0.292	$5.18^{+0.36}_{-0.29}$	$8.31^{+0.26}_{-0.22}$	$6.70^{+0.25}_{-0.25}$	$6.53^{+0.28}_{-0.28}$	$8.28^{+0.30}_{-0.30}$	$5.68^{+0.10}_{-0.10}$	$18.64^{+1.27}_{-1.27}$	$12.80^{+0.50}_{-0.50}$	4	0.51	14	0.78
G107.11+65.31	0.292	$7.26^{+0.75}_{-0.67}$	$6.94^{+0.30}_{-0.28}$	$6.64^{+0.49}_{-0.49}$	$6.78^{+0.69}_{-0.69}$	$10.02^{+0.56}_{-0.56}$	$9.03^{+0.42}_{-0.42}$	$27.55^{+3.06}_{-3.06}$	$24.83^{+2.38}_{-2.38}$	6	0.8	25	1.00
G113.82+44.35	0.225	$3.87^{+0.32}_{-0.21}$	$5.70^{+0.28}_{-0.22}$	$5.29^{+0.30}_{-0.30}$	$5.43^{+0.34}_{-0.34}$	$3.73^{+0.22}_{-0.22}$	$3.14^{+0.14}_{-0.14}$	$7.95^{+0.68}_{-0.68}$	$6.68^{+0.45}_{-0.45}$	4	0.64	19	0.89

Table 3
(Continued)

Planck Name	z	$M_{\rm tot}$ ($10^{14}\,M_{\odot}$)	$M_{\rm gas}$ ($10^{13}\,M_{\odot}$)	kT (keV)	$kT_{\rm exc}$ (keV)	$L_{\rm X}$ (erg s^{-1})	$L_{\rm X,exc}$ (erg s^{-1})	$L_{\rm bol}$ (erg s^{-1})	$L_{\rm bol,exc}$ (erg s^{-1})	N_T	f_T	$N_{\rm sb}$	$f_{\rm sb}$
G124.21–36.48	0.197	$5.81^{+0.57}_{-0.62}$	$7.81^{+0.29}_{-0.33}$	$4.78^{+0.11}_{-0.11}$	$5.81^{+0.16}_{-0.16}$	$3.89^{+0.14}_{-0.14}$	$2.42^{+0.06}_{-0.06}$	$7.91^{+0.34}_{-0.34}$	$4.94^{+0.16}_{-0.16}$	9	0.81	23	1.23
G125.70+53.85	0.302	$6.78^{+0.69}_{-0.65}$	$9.64^{+0.43}_{-0.43}$	$6.84^{+0.44}_{-0.44}$	$6.99^{+0.58}_{-0.58}$	$6.94^{+0.39}_{-0.39}$	$4.93^{+0.14}_{-0.14}$	$18.07^{+1.81}_{-1.81}$	$12.02^{+0.70}_{-0.70}$	5	0.96	14	1.15
G139.19+56.35	0.322	$7.42^{+5.68}_{-1.68}$	$10.23^{+1.42}_{-0.80}$	$6.10^{+0.57}_{-0.57}$	$6.32^{+0.69}_{-0.69}$	$6.47^{+0.56}_{-0.56}$	$5.45^{+0.38}_{-0.38}$	$16.18^{+1.83}_{-1.83}$	$13.66^{+1.07}_{-1.07}$	4	0.39	15	0.63
G149.73+34.69	0.182	$7.12^{+0.71}_{-0.63}$	$11.68^{+0.57}_{-0.55}$	$7.39^{+0.42}_{-0.42}$	$7.15^{+0.51}_{-0.51}$	$8.46^{+0.36}_{-0.36}$	$5.96^{+0.15}_{-0.15}$	$22.10^{+1.79}_{-1.79}$	$15.61^{+0.81}_{-0.81}$	6	0.59	11	0.72
G157.43+30.33	0.450	$6.23^{+0.52}_{-0.42}$	$9.64^{+0.35}_{-0.31}$	$7.54^{+0.58}_{-0.58}$	$7.06^{+0.59}_{-0.59}$	$8.01^{+0.27}_{-0.27}$	$6.15^{+0.23}_{-0.23}$	$21.05^{+1.57}_{-1.57}$	$16.26^{+1.14}_{-1.14}$	3	1.00	13	1.13
G159.85–73.47	0.206	$6.73^{+0.64}_{-0.70}$	$9.88^{+0.41}_{-0.47}$	$5.89^{+0.57}_{-0.57}$	$5.82^{+0.83}_{-0.83}$	$6.86^{+0.27}_{-0.27}$	$4.80^{+0.11}_{-0.11}$	$16.15^{+0.90}_{-0.90}$	$11.29^{+0.37}_{-0.37}$	10	1.09	34	1.09
G164.18–38.89*	0.074	$5.07^{+0.45}_{-0.22}$	$6.30^{+0.28}_{-0.15}$	$6.52^{+0.15}_{-0.15}$	$6.50^{+0.18}_{-0.18}$	$4.16^{+0.19}_{-0.19}$	$3.30^{+0.13}_{-0.13}$	$8.83^{+0.47}_{-0.47}$	$7.01^{+0.34}_{-0.34}$	13	0.70	66	1.01
G166.13+43.39	0.217	$6.86^{+0.48}_{-0.41}$	$8.68^{+0.22}_{-0.19}$	$6.56^{+0.21}_{-0.21}$	$6.30^{+0.29}_{-0.29}$	$6.83^{+0.22}_{-0.22}$	$4.18^{+0.11}_{-0.11}$	$16.37^{+0.51}_{-0.51}$	$10.02^{+0.37}_{-0.37}$	6	0.76	15	0.83
G167.65+17.64*	0.174	$5.88^{+0.40}_{-0.30}$	$9.25^{+0.26}_{-0.21}$	$6.28^{+0.20}_{-0.20}$	$6.02^{+0.23}_{-0.23}$	$6.41^{+0.25}_{-0.25}$	$4.74^{+0.11}_{-0.11}$	$13.84^{+0.76}_{-0.76}$	$10.24^{+0.36}_{-0.36}$	11	0.77	29	0.97
G171.94–40.65	0.270	$12.33^{+3.45}_{-2.12}$	$15.02^{+0.96}_{-0.75}$	$9.79^{+0.45}_{-0.45}$	$9.37^{+0.49}_{-0.49}$	$11.21^{+0.36}_{-0.36}$	$7.32^{+0.18}_{-0.18}$	$32.74^{+2.28}_{-2.28}$	$21.47^{+0.26}_{-0.26}$	4	0.34	11	0.54
G180.24+21.04	0.546	$12.58^{+0.53}_{-0.68}$	$23.47^{+0.36}_{-0.50}$	$10.12^{+0.25}_{-0.25}$	$9.96^{+0.27}_{-0.27}$	$23.81^{+0.78}_{-0.78}$	$17.95^{+0.47}_{-0.47}$	$72.74^{+3.61}_{-3.61}$	$54.55^{+2.36}_{-2.36}$	5	0.95	33	1.58
G182.44–28.29	0.088	$6.93^{+0.17}_{-0.18}$	$9.58^{+0.11}_{-0.20}$	$7.53^{+0.12}_{-0.12}$	$7.13^{+0.32}_{-0.32}$	$12.18^{+0.11}_{-0.11}$	$4.69^{+0.01}_{-0.01}$	$33.55^{+0.44}_{-0.44}$	$12.89^{+0.08}_{-0.08}$	26	0.99	65	1.10
G182.63+55.82	0.206	$4.77^{+0.26}_{-0.16}$	$6.88^{+0.15}_{-0.10}$	$5.71^{+0.11}_{-0.11}$	$5.54^{+0.15}_{-0.15}$	$6.06^{+0.20}_{-0.20}$	$3.18^{+0.07}_{-0.07}$	$13.90^{+0.65}_{-0.65}$	$7.28^{+0.25}_{-0.25}$	8	0.97	40	1.34
G186.39+37.25	0.282	$9.28^{+1.19}_{-0.89}$	$12.49^{+0.61}_{-0.52}$	$8.77^{+1.40}_{-1.40}$	$7.38^{+1.58}_{-1.58}$	$11.61^{+0.60}_{-0.60}$	$8.27^{+0.50}_{-0.50}$	$30.83^{+2.56}_{-2.56}$	$22.24^{+1.51}_{-1.51}$	1	0.57	4	0.84
G195.62+44.05	0.295	$5.82^{+0.72}_{-0.49}$	$8.77^{+0.49}_{-0.36}$	$5.26^{+0.13}_{-0.13}$	$5.26^{+0.15}_{-0.15}$	$4.82^{+0.21}_{-0.21}$	$4.10^{+0.15}_{-0.15}$	$10.30^{+0.58}_{-0.58}$	$8.77^{+0.43}_{-0.43}$	6	0.97	32	1.06
G195.77–24.30	0.203	$6.67^{+0.32}_{-0.22}$	$11.14^{+0.24}_{-0.16}$	$6.80^{+0.18}_{-0.18}$	$6.84^{+0.21}_{-0.21}$	$6.95^{+0.24}_{-0.24}$	$5.84^{+0.19}_{-0.19}$	$17.45^{+1.03}_{-1.03}$	$14.67^{+0.81}_{-0.81}$	12	1.03	47	1.26
G218.85+35.50	0.175	$3.86^{+0.45}_{-0.41}$	$4.30^{+0.20}_{-0.19}$	$4.48^{+0.31}_{-0.31}$	$4.17^{+0.54}_{-0.54}$	$3.05^{+0.17}_{-0.17}$	$1.72^{+0.06}_{-0.06}$	$6.52^{+0.46}_{-0.46}$	$3.68^{+0.18}_{-0.18}$	5	0.44	26	1.14
G225.92–19.99	0.460	$11.07^{+3.23}_{-4.48}$	$21.96^{+2.86}_{-5.42}$	$7.01^{+0.33}_{-0.33}$	$7.46^{+0.42}_{-0.42}$	$22.54^{+1.69}_{-1.69}$	$16.54^{+1.24}_{-1.24}$	$56.88^{+5.50}_{-5.50}$	$41.61^{+3.16}_{-3.16}$	4	0.90	34	1.07
G226.17–21.91	0.099	$4.61^{+0.32}_{-0.23}$	$5.10^{+0.11}_{-0.09}$	$4.85^{+0.11}_{-0.11}$	$4.65^{+0.14}_{-0.14}$	$3.31^{+0.12}_{-0.12}$	$2.38^{+0.07}_{-0.07}$	$6.95^{+0.34}_{-0.34}$	$4.99^{+0.20}_{-0.20}$	14	0.94	46	0.99
G226.24+76.76	0.143	$6.28^{+0.12}_{-0.09}$	$8.34^{+0.06}_{-0.05}$	$7.03^{+0.06}_{-0.06}$	$6.89^{+0.08}_{-0.08}$	$6.83^{+0.10}_{-0.10}$	$3.26^{+0.02}_{-0.02}$	$17.63^{+0.35}_{-0.35}$	$8.40^{+0.07}_{-0.07}$	10	1.11	58	1.31
G228.15+75.19	0.545	$7.94^{+0.96}_{-0.60}$	$13.54^{+0.78}_{-0.57}$	$9.46^{+0.69}_{-0.69}$	$9.20^{+0.78}_{-0.78}$	$15.35^{+0.78}_{-0.78}$	$9.64^{+0.42}_{-0.42}$	$43.85^{+3.43}_{-3.43}$	$34.24^{+1.67}_{-1.67}$	3	1.07	17	1.16
G228.49+53.12	0.143	$5.16^{+0.35}_{-0.42}$	$5.87^{+0.17}_{-0.21}$	$5.29^{+0.17}_{-0.17}$	$5.54^{+0.37}_{-0.37}$	$4.76^{+0.16}_{-0.16}$	$1.93^{+0.03}_{-0.03}$	$10.23^{+0.46}_{-0.46}$	$4.16^{+0.11}_{-0.11}$	7	0.94	29	1.26
G229.21–17.24	0.171	$5.26^{+1.84}_{-1.19}$	$6.56^{+0.84}_{-0.68}$	$5.72^{+0.28}_{-0.28}$	$5.65^{+0.35}_{-0.35}$	$2.90^{+0.17}_{-0.17}$	$2.33^{+0.06}_{-0.06}$	$6.39^{+0.52}_{-0.52}$	$5.14^{+0.26}_{-0.26}$	8	0.75	20	0.81
G229.94+15.29	0.070	$7.01^{+0.25}_{-0.26}$	$8.51^{+0.12}_{-0.13}$	$6.94^{+0.15}_{-0.15}$	$6.79^{+0.28}_{-0.28}$	$5.62^{+0.09}_{-0.09}$	$2.80^{+0.02}_{-0.02}$	$14.67^{+0.35}_{-0.35}$	$7.30^{+0.11}_{-0.11}$	17	1.17	163	1.43
G236.95–26.67	0.148	$5.91^{+0.32}_{-0.33}$	$6.96^{+0.14}_{-0.14}$	$5.79^{+0.13}_{-0.13}$	$5.57^{+0.17}_{-0.17}$	$3.96^{+0.14}_{-0.14}$	$2.42^{+0.05}_{-0.05}$	$9.20^{+0.43}_{-0.43}$	$5.61^{+0.20}_{-0.20}$	10	0.83	52	0.79
G241.74–30.88	0.271	$5.80^{+0.42}_{-0.33}$	$7.59^{+0.25}_{-0.22}$	$6.98^{+0.35}_{-0.35}$	$6.75^{+0.52}_{-0.52}$	$8.14^{+0.28}_{-0.28}$	$4.62^{+0.11}_{-0.11}$	$19.94^{+1.15}_{-1.15}$	$11.32^{+0.52}_{-0.52}$	4	0.91	15	1.03
G241.77–24.00	0.139	$3.29^{+0.06}_{-0.06}$	$3.95^{+0.04}_{-0.04}$	$4.55^{+0.06}_{-0.06}$	$4.93^{+0.12}_{-0.12}$	$4.74^{+0.14}_{-0.14}$	$2.10^{+0.07}_{-0.07}$	$9.89^{+0.32}_{-0.32}$	$4.43^{+0.15}_{-0.15}$	9	0.84	48	1.01
G241.97+14.85	0.169	$4.13^{+0.64}_{-0.38}$	$7.10^{+0.69}_{-0.45}$	$6.12^{+0.10}_{-0.10}$	$6.23^{+0.11}_{-0.11}$	$4.88^{+0.33}_{-0.33}$	$3.08^{+0.18}_{-0.18}$	$10.54^{+0.82}_{-0.82}$	$6.66^{+0.47}_{-0.47}$	14	1.15	33	1.51
G244.34–32.13	0.284	$6.94^{+0.54}_{-0.50}$	$11.46^{+0.39}_{-0.38}$	$7.02^{+0.29}_{-0.29}$	$7.25^{+0.41}_{-0.41}$	$10.30^{+0.39}_{-0.39}$	$6.93^{+0.21}_{-0.21}$	$24.97^{+1.74}_{-1.74}$	$16.90^{+1.06}_{-1.06}$	5	0.90	11	0.94
G244.69+32.49	0.153	$3.70^{+0.31}_{-0.19}$	$5.04^{+0.17}_{-0.12}$	$5.20^{+0.26}_{-0.26}$	$5.01^{+0.29}_{-0.29}$	$3.18^{+0.13}_{-0.13}$	$2.39^{+0.08}_{-0.08}$	$6.54^{+0.46}_{-0.46}$	$4.91^{+0.30}_{-0.30}$	5	0.63	11	0.70
G247.17–23.32	0.152	$3.17^{+0.54}_{-0.35}$	$4.16^{+0.37}_{-0.26}$	$4.45^{+0.24}_{-0.24}$	$4.65^{+0.38}_{-0.38}$	$2.49^{+0.14}_{-0.14}$	$1.81^{+0.08}_{-0.08}$	$4.84^{+0.40}_{-0.40}$	$3.51^{+0.25}_{-0.25}$	7	1.01	17	1.01
G249.87–39.86	0.165	$2.86^{+0.56}_{-0.40}$	$4.02^{+0.36}_{-0.28}$	$3.97^{+0.22}_{-0.22}$	$3.91^{+0.33}_{-0.33}$	$2.33^{+0.10}_{-0.10}$	$1.51^{+0.04}_{-0.04}$	$3.91^{+0.24}_{-0.24}$	$2.53^{+0.10}_{-0.10}$	5	0.51	15	0.84
G250.90–36.25	0.200	$5.36^{+0.51}_{-0.36}$	$6.74^{+0.27}_{-0.20}$	$5.98^{+0.23}_{-0.23}$	$5.97^{+0.36}_{-0.36}$	$4.91^{+0.18}_{-0.18}$	$2.93^{+0.08}_{-0.08}$	$11.18^{+0.66}_{-0.66}$	$6.67^{+0.31}_{-0.31}$	6	0.83	21	0.83
G252.96–56.05	0.075	$3.58^{+0.04}_{-0.05}$	$3.90^{+0.03}_{-0.03}$	$4.10^{+0.03}_{-0.03}$	$4.37^{+0.08}_{-0.08}$	$3.85^{+0.04}_{-0.04}$	$1.49^{+0.01}_{-0.01}$	$7.42^{+0.10}_{-0.10}$	$2.88^{+0.01}_{-0.01}$	15	0.60	133	0.77
G253.47–33.72	0.191	$4.52^{+0.44}_{-0.48}$	$5.71^{+0.30}_{-0.33}$	$5.96^{+0.38}_{-0.38}$	$5.76^{+0.52}_{-0.52}$	$3.56^{+0.18}_{-0.18}$	$2.48^{+0.11}_{-0.11}$	$8.59^{+0.70}_{-0.70}$	$5.98^{+0.43}_{-0.43}$	6	1.00	16	1.07
G256.45–65.71	0.220	$5.42^{+0.89}_{-0.76}$	$7.18^{+0.57}_{-0.54}$	$4.94^{+0.19}_{-0.19}$	$5.73^{+0.33}_{-0.33}$	$5.74^{+0.25}_{-0.25}$	$3.63^{+0.12}_{-0.12}$	$11.96^{+0.72}_{-0.72}$	$7.54^{+0.38}_{-0.38}$	7	1.01	22	1.17
G257.34–22.18	0.203	$3.19^{+0.88}_{-0.51}$	$4.51^{+0.82}_{-0.51}$	$1.67^{+1.34}_{-1.34}$	$1.40^{+1.33}_{-1.33}$	$2.76^{+0.34}_{-0.34}$	$2.43^{+0.31}_{-0.31}$	$6.09^{+1.06}_{-1.06}$	$5.37^{+0.94}_{-0.94}$	2	0.35	11	0.82
G260.03–63.44	0.284	$7.15^{+0.73}_{-0.73}$	$10.03^{+0.33}_{-0.29}$	$6.43^{+0.18}_{-0.18}$	$6.76^{+0.28}_{-0.28}$	$12.55^{+0.26}_{-0.26}$	$7.60^{+0.01}_{-0.01}$	$28.88^{+1.13}_{-1.13}$	$17.53^{+0.26}_{-0.26}$	5	0.72	22	1.17
G262.25–35.36	0.295	$6.59^{+0.90}_{-0.70}$	$10.80^{+0.78}_{-0.67}$	$7.90^{+0.19}_{-0.19}$	$7.86^{+0.20}_{-0.20}$	$6.94^{+0.37}_{-0.37}$	$5.89^{+0.28}_{-0.28}$	$17.22^{+1.60}_{-1.60}$	$14.66^{+1.26}_{-1.26}$	5	0.68	12	0.95
G262.71–40.91	0.420	$9.16^{+2.11}_{-1.59}$	$12.29^{+0.78}_{-0.69}$	$9.33^{+0.39}_{-0.39}$	$10.08^{+0.68}_{-0.68}$	$12.84^{+0.44}_{-0.44}$	$6.69^{+0.16}_{-0.16}$	$36.85^{+2.32}_{-2.32}$	$19.17^{+0.10}_{-0.10}$	3	0.44	12	0.75
G263.16–23.41	0.227	$7.07^{+0.35}_{-0.28}$	$11.22^{+0.22}_{-0.18}$	$7.18^{+0.16}_{-0.16}$	$7.43^{+0.26}_{-0.26}$	$10.55^{+0.34}_{-0.34}$	$5.49^{+0.12}_{-0.12}$	$27.27^{+1.28}_{-1.28}$	$14.18^{+0.54}_{-0.54}$	8	0.97	45	1.06
G263.66–22.53	0.164	$8.59^{+0.65}_{-0.45}$	$10.52^{+0.29}_{-0.21}$	$7.10^{+0.18}_{-0.18}$	$7.22^{+0.28}_{-0.28}$	$6.55^{+0.23}_{-0.23}$	$4.08^{+0.11}_{-0.11}$	$16.83^{+0.88}_{-0.88}$	$10.48^{+0.47}_{-0.47}$	10	1.05	34	1.12

Table 3
(Continued)

Planck Name	z	$M_{\rm tot}$ ($10^{14}\,M_\odot$)	$M_{\rm gas}$ ($10^{13}\,M_\odot$)	kT (keV)	$kT_{\rm exc}$ (keV)	$L_{\rm X}$ (erg s^{-1})	$L_{\rm X,exc}$ (erg s^{-1})	$L_{\rm bol}$ (erg s^{-1})	$L_{\rm bol,exc}$ (erg s^{-1})	N_T	f_T	$N_{\rm sb}$	$f_{\rm sb}$
G266.03–21.25	0.296	$12.56^{+0.34}_{-0.34}$	$21.79^{+0.22}_{-0.23}$	$10.57^{+0.26}_{-0.26}$	$10.66^{+0.34}_{-0.34}$	$21.79^{+0.68}_{-0.68}$	$15.16^{+0.38}_{-0.38}$	$65.46^{+2.90}_{-2.90}$	$45.55^{+1.78}_{-1.78}$	10	1.03	59	1.32
G269.31–49.87	0.085	$2.65^{+0.41}_{-0.23}$	$3.19^{+0.26}_{-0.16}$	$4.82^{+0.25}_{-0.25}$	$4.93^{+0.39}_{-0.39}$	$1.62^{+0.08}_{-0.08}$	$1.07^{+0.03}_{-0.03}$	$3.34^{+0.25}_{-0.25}$	$2.20^{+0.14}_{-0.14}$	7	0.73	34	0.83
G271.19–30.96	0.370	$8.38^{+0.68}_{-0.53}$	$12.80^{+0.49}_{-0.52}$	$8.22^{+0.24}_{-0.24}$	$8.80^{+0.46}_{-0.46}$	$19.29^{+0.67}_{-0.67}$	$8.19^{+0.03}_{-0.03}$	$52.15^{+3.21}_{-3.21}$	$22.16^{+0.49}_{-0.49}$	3	0.37	17	0.54
G271.50–56.55	0.300	$8.07^{+2.11}_{-1.51}$	$9.79^{+0.75}_{-0.61}$	$7.10^{+0.71}_{-0.71}$	$7.02^{+0.91}_{-0.91}$	$8.44^{+0.62}_{-0.62}$	$5.18^{+0.35}_{-0.35}$	$24.85^{+1.97}_{-1.97}$	$16.30^{+1.21}_{-1.21}$	4	0.57	36	0.83
G272.10–40.15	0.059	$6.11^{+0.09}_{-0.08}$	$7.79^{+0.05}_{-0.05}$	$6.35^{+0.04}_{-0.04}$	$6.10^{+0.04}_{-0.04}$	$5.02^{+0.08}_{-0.08}$	$4.01^{+0.06}_{-0.06}$	$12.62^{+0.29}_{-0.29}$	$10.10^{+0.21}_{-0.21}$	33	0.89	372	0.95
G277.75–51.73	0.440	$8.96^{+0.73}_{-0.59}$	$14.49^{+0.54}_{-0.47}$	$7.80^{+0.23}_{-0.23}$	$7.74^{+0.25}_{-0.25}$	$9.41^{+0.38}_{-0.38}$	$8.20^{+0.29}_{-0.29}$	$25.18^{+1.51}_{-1.51}$	$21.96^{+1.21}_{-1.21}$	6	1.01	25	1.35
G278.60+39.17	0.307	$9.37^{+0.87}_{-0.81}$	$13.38^{+0.56}_{-0.55}$	$8.02^{+0.35}_{-0.35}$	$7.98^{+0.46}_{-0.46}$	$10.53^{+0.38}_{-0.38}$	$7.50^{+0.26}_{-0.26}$	$26.14^{+1.23}_{-1.23}$	$18.64^{+0.80}_{-0.80}$	6	0.93	17	1.04
G280.19+47.81	0.156	$6.53^{+1.70}_{-1.09}$	$7.44^{+0.61}_{-0.47}$	$6.99^{+0.26}_{-0.26}$	$6.94^{+0.32}_{-0.32}$	$3.13^{+0.16}_{-0.16}$	$2.50^{+0.06}_{-0.06}$	$7.48^{+0.55}_{-0.55}$	$5.99^{+0.27}_{-0.27}$	8	0.66	22	0.89
G282.49+65.17	0.077	$5.25^{+0.22}_{-0.20}$	$6.64^{+0.11}_{-0.10}$	$5.54^{+0.14}_{-0.14}$	$5.41^{+0.18}_{-0.18}$	$2.97^{+0.05}_{-0.05}$	$2.19^{+0.02}_{-0.02}$	$6.82^{+0.18}_{-0.18}$	$5.02^{+0.11}_{-0.11}$	16	1.05	141	1.12
G283.16–22.93	0.450	$7.34^{+1.14}_{-0.97}$	$10.53^{+0.65}_{-0.61}$	$7.32^{+0.36}_{-0.36}$	$7.52^{+0.49}_{-0.49}$	$9.94^{+0.39}_{-0.39}$	$6.47^{+0.27}_{-0.27}$	$26.47^{+1.30}_{-1.30}$	$17.22^{+0.77}_{-0.77}$	3	0.99	9	1.02
G284.46+52.43	0.441	$10.63^{+0.55}_{-0.48}$	$16.94^{+0.34}_{-0.31}$	$9.48^{+0.14}_{-0.14}$	$9.83^{+0.21}_{-0.21}$	$20.29^{+0.43}_{-0.43}$	$12.07^{+0.38}_{-0.38}$	$63.47^{+1.53}_{-1.53}$	$37.68^{+1.10}_{-1.10}$	7	0.98	59	1.51
G284.99–23.70*	0.390	$10.10^{+1.57}_{-1.23}$	$14.88^{+0.83}_{-0.70}$	$7.53^{+0.53}_{-0.53}$	$7.61^{+0.78}_{-0.78}$	$17.51^{+0.83}_{-0.83}$	$9.85^{+0.22}_{-0.22}$	$41.13^{+2.89}_{-2.89}$	$23.17^{+1.06}_{-1.06}$	3	0.36	16	0.62
G285.63–17.24*	0.350	$6.59^{+1.00}_{-1.17}$	$8.20^{+0.57}_{-0.78}$	$5.78^{+0.63}_{-0.63}$	$5.74^{+0.68}_{-0.68}$	$3.98^{+0.40}_{-0.40}$	$3.35^{+0.30}_{-0.30}$	$7.80^{+1.09}_{-1.09}$	$6.56^{+0.85}_{-0.85}$	1	0.86	14	0.86
G286.58–31.25	0.210	$5.52^{+0.45}_{-0.26}$	$7.18^{+0.24}_{-0.15}$	$5.88^{+0.15}_{-0.15}$	$5.87^{+0.19}_{-0.19}$	$4.08^{+0.13}_{-0.13}$	$3.07^{+0.08}_{-0.08}$	$9.28^{+0.44}_{-0.44}$	$7.00^{+0.29}_{-0.29}$	7	1.01	30	1.21
G286.99+32.91	0.390	$12.20^{+0.76}_{-0.70}$	$22.08^{+0.62}_{-0.57}$	$10.62^{+0.69}_{-0.69}$	$10.47^{+0.73}_{-0.73}$	$19.86^{+0.77}_{-0.77}$	$15.63^{+0.53}_{-0.53}$	$62.75^{+4.77}_{-4.77}$	$49.38^{+3.45}_{-3.45}$	5	1.03	12	1.09
G288.61–37.65	0.127	$4.00^{+0.70}_{-0.48}$	$7.35^{+0.67}_{-0.50}$	$3.09^{+0.93}_{-0.93}$	$2.38^{+1.10}_{-1.10}$	$5.26^{+0.32}_{-0.32}$	$3.60^{+0.19}_{-0.19}$	$12.77^{+1.00}_{-1.00}$	$8.75^{+0.61}_{-0.61}$	5	1.03	33	1.06
G292.51+21.98	0.300	$8.03^{+0.49}_{-0.44}$	$11.39^{+0.29}_{-0.27}$	$7.53^{+0.88}_{-0.88}$	$7.22^{+0.50}_{-0.50}$	$6.41^{+0.36}_{-0.36}$	$5.65^{+0.30}_{-0.30}$	$15.97^{+1.25}_{-1.25}$	$14.08^{+1.06}_{-1.06}$	6	0.69	33	1.05
G294.66–37.02	0.274	$7.20^{+0.59}_{-0.39}$	$9.88^{+0.36}_{-0.26}$	$7.88^{+0.30}_{-0.30}$	$7.80^{+0.39}_{-0.39}$	$8.05^{+0.44}_{-0.44}$	$5.93^{+0.28}_{-0.28}$	$22.32^{+2.01}_{-2.01}$	$16.46^{+1.37}_{-1.37}$	4	0.97	14	1.09
G304.67–31.66	0.193	$4.16^{+1.10}_{-0.79}$	$5.38^{+0.76}_{-0.61}$	$5.15^{+0.69}_{-0.69}$	$5.22^{+0.96}_{-0.96}$	$2.41^{+0.46}_{-0.46}$	$2.15^{+0.43}_{-0.43}$	$4.54^{+1.07}_{-1.07}$	$4.02^{+1.00}_{-1.00}$	2	0.67	5	0.90
G304.84–41.42	0.410	$8.28^{+0.64}_{-0.60}$	$11.41^{+0.38}_{-0.35}$	$9.47^{+1.31}_{-1.31}$	$8.73^{+1.22}_{-1.22}$	$10.21^{+0.26}_{-0.26}$	$7.14^{+0.35}_{-0.35}$	$23.76^{+1.16}_{-1.16}$	$16.56^{+0.91}_{-0.91}$	2	0.95	6	0.95
G306.68+61.06	0.085	$3.93^{+0.13}_{-0.31}$	$5.03^{+0.07}_{-0.17}$	$5.00^{+0.10}_{-0.10}$	$4.78^{+0.15}_{-0.15}$	$3.93^{+0.07}_{-0.07}$	$2.32^{+0.01}_{-0.01}$	$8.36^{+0.19}_{-0.19}$	$4.93^{+0.05}_{-0.05}$	22	1.02	144	1.02
G306.80+58.60	0.085	$4.60^{+0.26}_{-0.16}$	$5.82^{+0.14}_{-0.09}$	$5.64^{+0.11}_{-0.11}$	$5.58^{+0.15}_{-0.15}$	$4.46^{+0.07}_{-0.07}$	$2.61^{+0.04}_{-0.04}$	$10.62^{+0.22}_{-0.22}$	$6.23^{+0.10}_{-0.10}$	17	0.98	72	1.04
G308.32–20.23*	0.480	$8.61^{+1.22}_{-0.98}$	$10.52^{+0.57}_{-0.48}$	$8.95^{+0.84}_{-0.84}$	$7.40^{+0.70}_{-0.70}$	$17.31^{+1.14}_{-1.14}$	$10.39^{+0.43}_{-0.43}$	$67.99^{+7.98}_{-7.98}$	$40.90^{+3.79}_{-3.79}$	3	0.66	21	0.66
G313.36+61.11	0.183	$7.87^{+0.10}_{-0.09}$	$10.53^{+0.07}_{-0.06}$	$8.60^{+0.08}_{-0.08}$	$8.26^{+0.11}_{-0.11}$	$12.82^{+0.13}_{-0.13}$	$5.47^{+0.14}_{-0.14}$	$37.61^{+0.68}_{-0.68}$	$16.14^{+0.13}_{-0.13}$	9	0.98	80	1.01
G313.87–17.10	0.153	$8.24^{+0.25}_{-0.23}$	$10.78^{+0.13}_{-0.13}$	$8.43^{+0.15}_{-0.15}$	$8.15^{+0.24}_{-0.24}$	$11.10^{+0.33}_{-0.33}$	$5.57^{+0.15}_{-0.15}$	$31.84^{+1.60}_{-1.60}$	$15.91^{+0.77}_{-0.77}$	11	0.91	61	0.91
G318.13–29.57	0.217	$5.59^{+0.64}_{-0.57}$	$7.43^{+0.40}_{-0.38}$	$5.96^{+0.66}_{-0.66}$	$5.17^{+0.93}_{-0.93}$	$7.39^{+0.56}_{-0.56}$	$4.40^{+0.29}_{-0.29}$	$22.10^{+3.07}_{-3.07}$	$13.15^{+1.67}_{-1.67}$	2	0.83	4	1.11
G321.96–47.97	0.094	$3.95^{+0.29}_{-0.23}$	$4.83^{+0.17}_{-0.14}$	$4.60^{+0.11}_{-0.11}$	$4.43^{+0.14}_{-0.14}$	$3.10^{+0.09}_{-0.09}$	$2.33^{+0.05}_{-0.05}$	$6.51^{+0.23}_{-0.23}$	$4.91^{+0.15}_{-0.15}$	19	0.84	52	1.12
G324.49–44.97	0.095	$3.09^{+0.40}_{-0.19}$	$3.47^{+0.20}_{-0.10}$	$4.08^{+0.12}_{-0.12}$	$4.16^{+0.18}_{-0.18}$	$1.85^{+0.08}_{-0.08}$	$1.26^{+0.04}_{-0.04}$	$3.46^{+0.20}_{-0.20}$	$2.36^{+0.11}_{-0.11}$	10	0.99	37	1.08
G332.23–46.36	0.098	$5.09^{+0.15}_{-0.10}$	$7.06^{+0.08}_{-0.06}$	$6.13^{+0.09}_{-0.09}$	$5.95^{+0.12}_{-0.12}$	$4.71^{+0.11}_{-0.11}$	$3.09^{+0.06}_{-0.06}$	$11.37^{+0.34}_{-0.34}$	$7.48^{+0.20}_{-0.20}$	17	1.04	102	1.08
G332.88–19.28	0.147	$6.22^{+0.38}_{-0.33}$	$7.74^{+0.21}_{-0.19}$	$6.02^{+0.77}_{-0.77}$	$5.48^{+1.09}_{-1.09}$	$4.55^{+0.19}_{-0.19}$	$3.09^{+0.11}_{-0.11}$	$11.06^{+0.82}_{-0.82}$	$7.51^{+0.50}_{-0.50}$	6	0.47	13	0.58
G335.59–46.46	0.076	$3.53^{+0.74}_{-0.56}$	$4.61^{+0.54}_{-0.44}$	$4.17^{+1.20}_{-1.20}$	$3.95^{+1.36}_{-1.36}$	$4.19^{+0.32}_{-0.32}$	$3.53^{+0.25}_{-0.25}$	$10.13^{+0.94}_{-0.94}$	$8.55^{+0.75}_{-0.75}$	22	0.92	23	0.92
G336.59–55.44	0.097	$3.78^{+0.71}_{-0.52}$	$4.88^{+0.46}_{-0.36}$	$4.69^{+0.24}_{-0.24}$	$4.48^{+0.26}_{-0.26}$	$2.53^{+0.10}_{-0.10}$	$2.04^{+0.05}_{-0.05}$	$5.36^{+0.26}_{-0.26}$	$4.32^{+0.15}_{-0.15}$	20	1.05	23	1.19
G337.09–25.97	0.260	$5.75^{+0.50}_{-0.41}$	$8.94^{+0.34}_{-0.30}$	$5.67^{+0.22}_{-0.22}$	$5.86^{+0.36}_{-0.36}$	$6.57^{+0.25}_{-0.25}$	$3.61^{+0.06}_{-0.06}$	$14.33^{+0.80}_{-0.80}$	$7.87^{+0.28}_{-0.28}$	5	0.56	21	1.16
G342.31–34.90	0.232	$6.85^{+0.74}_{-0.62}$	$9.49^{+0.45}_{-0.40}$	$6.48^{+1.07}_{-1.07}$	$6.35^{+1.33}_{-1.33}$	$4.64^{+0.44}_{-0.44}$	$3.64^{+0.35}_{-0.35}$	$13.17^{+2.16}_{-2.16}$	$10.34^{+1.71}_{-1.71}$	2	0.59	13	0.92
G347.18–27.35	0.237	$8.24^{+0.63}_{-0.73}$	$11.07^{+0.43}_{-0.50}$	$8.31^{+0.40}_{-0.40}$	$8.16^{+0.51}_{-0.51}$	$5.63^{+0.31}_{-0.31}$	$4.56^{+0.19}_{-0.19}$	$15.15^{+1.21}_{-1.21}$	$12.25^{+0.81}_{-0.81}$	8	0.96	24	1.21
G349.46–59.94	0.347	$13.59^{+0.68}_{-0.65}$	$22.38^{+0.44}_{-0.42}$	$10.30^{+0.22}_{-0.22}$	$10.60^{+0.31}_{-0.31}$	$27.09^{+0.38}_{-0.38}$	$13.37^{+0.03}_{-0.03}$	$86.74^{+2.35}_{-2.35}$	$42.79^{+0.39}_{-0.39}$	7	1.00	47	1.14

Note. Column (1): Planck cluster name as in the Planck ESZ Catalog (Planck Collaboration et al. 2011). Column (2): cluster redshift. Columns (3)–(4): total and gas mass within R_{500}. Columns (5)–(6): core-included and core-excluded cluster temperature. Columns (7)–(8): core-included and core-excluded cluster luminosity in the soft band (0.1–2.4 keV). Columns (9)–(10): core-included and core-excluded cluster bolometric luminosity (0.01–100 keV). Column (11): number of bins in the temperature profile. Column (12): fraction of R_{500} covered by the temperature profile. Column (13): number of bins in the SB profile. Column (14): fraction of R_{500} covered by the SB profile.

(This table is available in machine-readable form.)

Table 4
Comparison between the Different Fitting Methods

Relation (Y–X)	Estimator	Fitted	α	β	γ	$\sigma_{X\|Z}$	$\sigma_{Y\|Z}$
L_X–M_{tot}	LIRA	β, γ, $\sigma_{X\|Z}$	0.089 ± 0.015	1.822 ± 0.246	0.462 ± 0.916	0.061 ± 0.021	0.082 ± 0.040
	LIRA	β, $\sigma_{X\|Z}$	0.081 ± 0.013	1.455 ± 0.098	[2]	0.025 ± 0.015	0.123 ± 0.014
	LIRA	β	0.080 ± 0.013	1.409 ± 0.077	[2]	[0]	0.129 ± 0.010
	LIRA	⋯	0.076 ± 0.014	[1]	[2]	0.015 ± 0.008	0.149 ± 0.011
	LIRA	β, $\sigma_{X\|Z}$	0.094 ± 0.015	1.949 ± 0.127	[0]	0.069 ± 0.010	0.049 ± 0.031
	BCES YX	β	-0.009 ± 0.013	1.500 ± 0.080	[2]	[0]	[0]
	BCES orth	β	-0.008 ± 0.014	1.740 ± 0.094	[2]	[0]	[0]
	LINMIX	β	-0.001 ± 0.013	1.427 ± 0.077	[2]	[0]	0.129 ± 0.051
$L_{X,exc}$–M_{tot}	LIRA	β, γ, $\sigma_{X\|Z}$	-0.091 ± 0.013	1.668 ± 0.183	1.325 ± 0.804	0.063 ± 0.015	0.034 ± 0.029
	LIRA	β, $\sigma_{X\|Z}$	-0.095 ± 0.011	1.525 ± 0.113	[2]	0.052 ± 0.016	0.063 ± 0.028
	LIRA	β	-0.097 ± 0.011	1.357 ± 0.064	[2]	[0]	0.104 ± 0.008
	LIRA	⋯	-0.100 ± 0.012	[1]	[2]	0.018 ± 0.008	0.123 ± 0.009
	LIRA	β, $\sigma_{X\|Z}$	-0.087 ± 0.013	1.872 ± 0.089	[0]	0.067 ± 0.006	0.022 ± 0.014
	BCES YX	β	-0.201 ± 0.011	1.390 ± 0.077	[2]	[0]	[0]
	BCES orth	β	-0.200 ± 0.011	1.540 ± 0.073	[2]	[0]	[0]
	LINMIX	β	-0.182 ± 0.011	1.375 ± 0.064	[2]	[0]	0.104 ± 0.042
L_X–T	LIRA	β, γ, $\sigma_{X\|Z}$	-0.250 ± 0.045	3.110 ± 0.422	0.398 ± 0.939	0.051 ± 0.010	0.052 ± 0.041
	LIRA	β, $\sigma_{X\|Z}$	-0.228 ± 0.032	2.862 ± 0.261	[1]	0.047 ± 0.009	0.080 ± 0.036
	LIRA	β	-0.168 ± 0.021	2.288 ± 0.137	[1]	⋯	0.150 ± 0.011
	LIRA	⋯	-0.084 ± 0.016	[1.5]	[1]	0.016 ± 0.007	0.174 ± 0.012
	LIRA	β, $\sigma_{X\|Z}$	-0.264 ± 0.028	3.237 ± 0.207	[0]	0.053 ± 0.005	0.066 ± 0.027
	BCES YX	β	-0.176 ± 0.033	2.070 ± 0.209	[1]	[0]	[0]
	BCES orth	β	-0.253 ± 0.037	2.830 ± 0.240	[1]	[0]	[0]
	LINMIX	β	-0.242 ± 0.020	2.156 ± 0.132	[1]	[0]	0.145 ± 0.056
$L_{X,exc}$–T_{exc}	LIRA	β, γ, $\sigma_{X\|Z}$	-0.360 ± 0.031	2.409 ± 0.292	1.170 ± 0.822	0.038 ± 0.011	0.052 ± 0.031
	LIRA	β, $\sigma_{X\|Z}$	-0.390 ± 0.020	2.732 ± 0.143	[1]	0.043 ± 0.004	0.030 ± 0.018
	LIRA	β	-0.347 ± 0.016	2.292 ± 0.106	[1]	[0]	0.111 ± 0.009
	LIRA	⋯	-0.259 ± 0.014	[1.5]	[1]	0.015 ± 0.006	0.145 ± 0.011
	LIRA	β, $\sigma_{X\|Z}$	-0.410 ± 0.020	2.949 ± 0.147	[0]	0.045 ± 0.004	0.023 ± 0.014
	BCES YX	β	-0.331 ± 0.038	1.920 ± 0.273	[1]	[0]	[0]
	BCES orth	β	-0.387 ± 0.034	2.560 ± 0.226	[1]	[0]	[0]
	LINMIX	β	-0.416 ± 0.015	2.135 ± 0.101	[1]	[0]	0.106 ± 0.043
M_{tot}–T	LIRA	β, γ, $\sigma_{X\|Z}$	-0.171 ± 0.015	1.556 ± 0.137	0.179 ± 0.379	0.032 ± 0.010	0.036 ± 0.016
	LIRA	β, $\sigma_{X\|Z}$	-0.199 ± 0.012	1.843 ± 0.084	[−1]	0.040 ± 0.004	0.016 ± 0.008
	LIRA	β	-0.173 ± 0.010	1.591 ± 0.067	[−1]	[0]	0.068 ± 0.006
	LIRA	⋯	-0.162 ± 0.007	[1.5]	[−1]	0.031 ± 0.009	0.050 ± 0.012
	LIRA	β, $\sigma_{X\|Z}$	-0.176 ± 0.011	1.606 ± 0.085	[0]	0.035 ± 0.007	0.028 ± 0.014
	BCES YX	β	-0.110 ± 0.018	1.500 ± 0.116	[−1]	[0]	[0]
	BCES orth	β	-0.119 ± 0.018	1.610 ± 0.116	[−1]	[0]	[0]
	LINMIX	β	-0.130 ± 0.011	1.607 ± 0.067	[−1]	[0]	0.064 ± 0.028
M_{tot}–M_{gas}	LIRA	β, γ, $\sigma_{X\|Z}$	0.073 ± 0.007	0.802 ± 0.049	-0.317 ± 0.307	0.028 ± 0.015	0.043 ± 0.011
	LIRA	β, $\sigma_{X\|Z}$	0.057 ± 0.006	0.669 ± 0.027	[0]	0.014 ± 0.007	0.052 ± 0.004
	LIRA	β	0.057 ± 0.007	0.620 ± 0.030	[0]	[0]	0.160 ± 0.011
	LIRA	$\sigma_{X\|Z}$	0.097 ± 0.010	[1])	[0]	0.104 ± 0.008	0.123 ± 0.009
	BCES YX	β	0.081 ± 0.005	0.790 ± 0.025	[0]	[0]	[0]
	BCES orth	β	0.081 ± 0.005	0.079 ± 0.024	[0]	[0]	[0]
	LINMIX	β	0.080 ± 0.005	0.778 ± 0.023	[0]	[0]	0.047 ± 0.005
M_{tot}–Y_X	LIRA	β, γ, $\sigma_{X\|Z}$	-0.010 ± 0.005	0.540 ± 0.030	-0.292 ± 0.287	0.039 ± 0.023	0.039 ± 0.011
	LIRA	β, $\sigma_{X\|Z}$	-0.010 ± 0.005	0.549 ± 0.019	[−0.4]	0.047 ± 0.022	0.037 ± 0.010
	LIRA	β	-0.005 ± 0.006	0.516 ± 0.018	[−0.4]	⋯	0.235 ± 0.016
	LIRA	$\sigma_{X\|Z}$	-0.003 ± 0.006	0.6 (fix)	[−0.4]	0.097 ± 0.010	0.207 ± 0.015
	LIRA	β, $\sigma_{X\|Z}$	-0.011 ± 0.005	0.517 ± 0.082	[0]	0.024 ± 0.017	0.042 ± 0.006
	BCES YX	β	0.015 ± 0.005	0.544 ± 0.016	[−0.4]	[0]	[0]
	BCES orth	β	0.015 ± 0.005	0.540 ± 0.016	[−0.4]	[0]	[0]
	LINMIX	β	0.006 ± 0.005	0.538 ± 0.016	[−0.4]	⋯	0.043 ± 0.019

Note. In the third column we indicate the parameters that were left free to vary with the exception of α and $\sigma_{Y|Z}$, which were always free when appropriate.

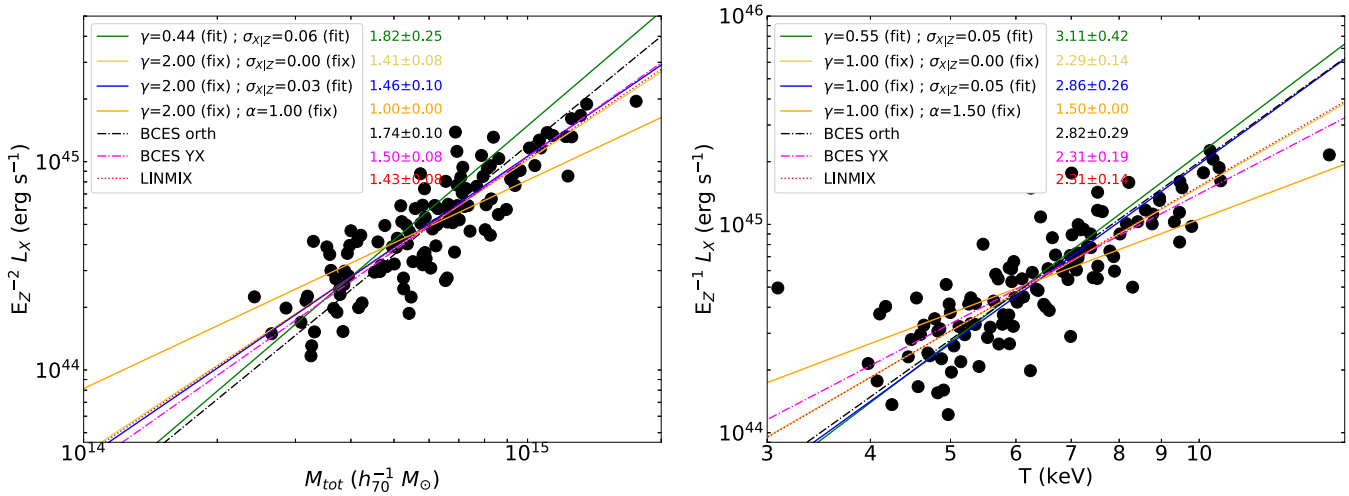

Figure 11. Left panel: lines show comparison of the fitted results for the L_X–M_{tot} relation obtained using different fitting methods. In green we show the fitted relation obtained using LIRA allowing all the parameters to vary (our reference model in the paper). In blue (intrinsic scatter in both variable) and yellow (intrinsic scatter only in the *Y*-axis) we show the best-fit results obtained assuming the self-similar redshift evolution (i.e., $\gamma = 2$). In orange we show the best fit obtained assuming that both the slope and the redshift evolution are self-similar. In black and magenta we show the result from BCES, while in red we show the result using the LINMIX algorithm. In both cases the redshift evolution was chosen to be self-similar. Right panel: same as in the left panel, but for the L_X–T relation.

determined in the fit with LIRA. Fixing the redshift evolution either to the self-similar value or to zero (i.e., redshift-independent relation) impacts the shape of the relations: the larger the γ factor, the flatter the relation (see Table 4). For all the relations, except M_{tot}–T, the fit prefers a γ value smaller than the self-similar prediction (although consistent within $\sim 1\sigma$). Although the significance for each relation is small, the systematic trend for all relations suggests that it is probably a real effect. Most relaxed clusters, which are thought to be less affected by processes such as gas motions, inhomogeneities, clumps, and shocks, show a redshift evolution more in agreement with the self-similar prediction, which strengthens our argument. However, if we assume that gravity is the only force driving structure formation, then we could fix the redshift evolution to the predictions and check if we can recover the predicted slopes. Fixing the redshift evolution tightens the relations, by breaking the degeneracy between α, β, and γ. In this case, the slope of the L_X–M_{tot} and L_X–T relations would be slightly flatter but still significantly steeper than the self-similar predictions. Also, the slopes of the M_{tot}–M_{gas} and M_{tot}–Y_X relations become flatter, but in this case the deviation from the self-similar prediction is even larger. The slope of the M_{tot}–T relation gets steeper than the self-similar prediction. Since the temperature of a cluster is only determined by the depth of its potential well, a deviation from self-similarity would require a mass bias that is temperature dependent. Considering the scatter in both variables can also play a significant role, depending on the distribution of the data points on the *X*-axis and on their errors and intrinsic scatter. In Figure 11 we show in blue and yellow the best-fit results obtained by fitting or not the intrinsic scatter in the *X*-axis. In the case of the L_X–T, the determined slopes are significantly different. When we set the scatter on *X* to zero, we find good agreement between LIRA and LINMIX.

Appendix C
Reproducibility of the Results

The R-package LIRA is a very powerful tool with many parameters that can be frozen or left free to vary depending on the analyses of interest (see Sereno 2016 for all the details). In this paper, we consider two main cases. In the first case, both the variables *X* and *Y* are treated as scattered proxy of an underlying quantity *Z*, e.g., the true mass or a rescaled version of the true mass. Here, $\sigma_{X|Z}$ and $\sigma_{Y|Z}$ are the intrinsic scatters of *X* and *Y* for a fixed value of *Z*. In the second case, we consider only the scatter in the *Y* variable, and $\sigma_{Y|Z=X}$ is the intrinsic scatter of *Y* for a given value of *X*.

To allow the full reproducibility of our results, below we provide the commands used in the different cases. Let `x` and `y`, `delta.x` and `delta.y`, `covariance.xy`, and `z` be the vectors storing the values of the observed x and y, their uncertainties δ_x and δ_y, the uncertainty covariance δ_{xy}, and the redshifts z, respectively. If not stated otherwise, priors and parameter values are set to default.

1. For regressions without scatter on the *X* variable, the analysis was performed with the command `> mcmc <- lira (x, y, delta.x = delta.x, delta.y = delta.y, covariance.xy = covariance.xy, z = z, z.ref = 0.2, gamma.mu.Z.Fz = 0.0, gamma.sigma.Z.D = 'dt', n.chains = 4, n.adapt = 2 × 10^3, n.iter = 2 × 10^4)`, where the covariate distribution is modeled as a Gaussian function with redshift evolving width (`gamma.sigma.Z.Fz = 'dt'`). Each of the `n.chains = 4` chains was `n.iter = 2 × 10^4` long, and the number of iterations for initialization was set to `n.adapt = 2 × 10^3`.
2. For regressions with scatter on the *X* variable, the analysis was performed with the command `> mcmc <- lira (x, y, delta.x = delta.x, delta.y = delta.y, covariance.xy = covariance.xy, z = z, z.ref = 0.2, sigma.XIZ.0 = 'prec.dgamma', gamma.mu.Z.Fz = 0.0, gamma.sigma.Z.D = 'dt,' n.chains = 4, n.adapt = 2 × 10^3, n.iter = 2 × 10^4)`, where the argument (`sigma.XIZ.0 = 'prec.dgamma'`) makes the scatter in *X* a parameter to be fitted.
3. For regressions with fixed time evolution, e.g., $\gamma = 2$, the analysis was performed with the command `> mcmc`

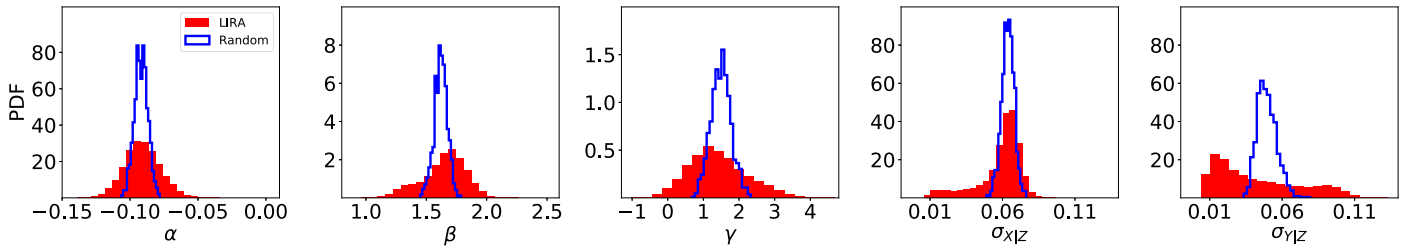

Figure 12. Comparison between the distributions of the parameters obtained using the Gibbs sampling used in LIRA (in blue) and the distribution obtained by perturbing the original data sets proportional to the observed measurement errors (in red).

`<- lira (x, y, delta.x = delta.x, delta.y = delta.y, covariance.xy = covariance.xy, z = z, z.ref = 0.2, gamma.YIZ = 2.0, gamma.mu.Z.Fz = 0.0, gamma.sigma.Z.D = 'dt', n.chains = 4, n.adapt = 2 × 10^3, n.iter = 2 × 10^4)`, where the argument `gamma.YIZ = 2` freezes γ to a fixed value.

4. For regressions with fixed time evolution and fixed slope, e.g., $\beta = 1$ and $\gamma = 2$, the analysis was performed with the command `> mcmc <- lira (x, y, delta.x = delta.x, delta.y = delta.y, covariance.xy = covariance.xy, z = z, z.ref = 0.2, beta.YIZ = 1.0, gamma.YIZ = 2.0, sigma.XIZ.0 = 'prec.dgamma', gamma.mu.Z.Fz = 0.0, gamma.sigma.Z.D = 'dt', n.chains = 4, n.adapt = 2 × 10^3, n.iter = 2 × 10^4)`, where the values of `beta.YIZ` and `gamma.YIZ` were frozen (`beta.YIZ = 1.0` and `gamma.YIZ = 2`).

Appendix D
Test the Underlying Assumptions of Our Regression Method

The LIRA software and its underlying assumptions and methods have been extensively tested with data and simulations (see, e.g., Sereno 2016 or Sereno et al. 2020). Accurate sampling of the parameter posterior probability distribution is crucial. Here we compare the LIRA sampling, which relies on Gibbs sampling exploiting the JAGS (Just Another Gibbs sampler) library,[10] with an alternative method where the original data set is perturbed proportional to the observed measurement errors, the fitting procedure is repeated for each random data extraction, and the parameter posterior is built as the distribution of the central momenta.

Let us consider the mass versus core-excised soft luminosity for the full sample in the more general case, e.g., time evolution and scatter in the X variable. We extracted a collection of 10^3 simulated data sets, where the random pairs $\{M_{500}$–$L_X\}$ are extracted from bi-variate Gaussians centered on the actual pair and with the same measured uncertainty covariance matrix. For each regression, we collect the posterior mean. As can be seen from Figure 12, there is good agreement between the two methods. The peaks of the posterior distributions are located well within the statistical uncertainty. The Gibbs sampling proves to be better suited to fully explore the full parameter space, with posterior generally broader.

[10] JAGS by M. Plummer is publicly available at http://mcmc-jags.sourceforge.net.

ORCID iDs

Lorenzo Lovisari https://orcid.org/0000-0002-3754-2415
Gerrit Schellenberger https://orcid.org/0000-0002-4962-0740
Mauro Sereno https://orcid.org/0000-0003-0302-0325
Stefano Ettori https://orcid.org/0000-0003-4117-8617
William R. Forman https://orcid.org/0000-0002-9478-1682
Christine Jones https://orcid.org/0000-0003-2206-4243
Felipe Andrade-Santos https://orcid.org/0000-0002-8144-9285
Scott Randall https://orcid.org/0000-0002-3984-4337
Ralph Kraft https://orcid.org/0000-0002-0765-0511

References

Akritas, M. G., & Bershady, M. A. 1996, ApJ, 470, 706
Anders, E., & Grevesse, N. 1989, GeCoA, 53, 197
Andrade-Santos, F., Jones, C., Forman, W. R., et al. 2017, ApJ, 843, 76
Arnaud, K. A. 1996, in ASP Conf. Ser. 101, Astronomical Data Analysis Software and Systems V, ed. G. H. Jacoby & J. Barnes (San Francisco, CA: ASP), 17
Arnaud, M., Pratt, G. W., Piffaretti, R., et al. 2010, A&A, 517, A92
Asplund, M., Grevesse, N., Sauval, A. J., & Scott, P. 2009, ARA&A, 47, 481
Bartalucci, I., Arnaud, M., Pratt, G. W., et al. 2017, A&A, 608, A88
Bartalucci, I., Arnaud, M., Pratt, G. W., Démoclès, J., & Lovisari, L. 2019, A&A, 628, A86
Bhattacharya, S., Habib, S., Heitmann, K., & Vikhlinin, A. 2013, ApJ, 766, 32
Böhringer, H., Schuecker, P., Pratt, G. W., et al. 2007, A&A, 469, 363
Bulbul, E., Chiu, I.-N., Mohr, J. J., et al. 2019, ApJ, 871, 50
Carlstrom, J. E., Ade, P. A. R., Aird, K. A., et al. 2011, PASP, 123, 568
Ettori, S. 2015, MNRAS, 446, 2629
Ettori, S., Tozzi, P., Borgani, S., & Rosati, P. 2004, A&A, 417, 13
Farahi, A., Mulroy, S. L., Evrard, A. E., et al. 2019, NatCo, 10, 2504
Gabriel, C., Denby, M., Fyfe, D. J., et al. 2004, in ASP Conf. Ser. 314, The XMM-Newton SAS—Distributed Development and Maintenance of a Large Science Analysis System: A Critical Analysis, ed. F. Ochsenbein, M. G. Allen, & D. Egret (San Francisco, CA: ASP), 759
Giles, P. A., Maughan, B. J., Pacaud, F., et al. 2016, A&A, 592, A3
Kelly, B. C. 2007, ApJ, 665, 1489
Kravtsov, A. V., Vikhlinin, A., & Nagai, D. 2006, ApJ, 650, 128
Le Brun, A. M. C., McCarthy, I. G., Schaye, J., & Ponman, T. J. 2017, MNRAS, 466, 4442
Leccardi, A., & Molendi, S. 2008, A&A, 486, 359
Lieu, M., Smith, G. P., Giles, P. A., et al. 2016, A&A, 592, A4
Lovisari, L., Forman, W. R., Jones, C., et al. 2017, ApJ, 846, 51
Lovisari, L., & Reiprich, T. H. 2019, MNRAS, 483, 540
Lovisari, L., Reiprich, T. H., & Schellenberger, G. 2015, A&A, 573, A118
Lovisari, L., Schindler, S., & Kapferer, W. 2011, A&A, 528, A60
Mahdavi, A., Hoekstra, H., Babul, A., et al. 2013, ApJ, 767, 116
Mantz, A., Allen, S. W., Ebeling, H., Rapetti, D., & Drlica-Wagner, A. 2010, MNRAS, 406, 1773
Mantz, A. B. 2016, MNRAS, 457, 1279
Mantz, A. B., Allen, S. W., Morris, R. G., et al. 2016, MNRAS, 463, 3582
Mantz, A. B., Allen, S. W., Morris, R. G., & von der Linden, A. 2018, MNRAS, 473, 3072
Martino, R., Mazzotta, P., Bourdin, H., et al. 2014, MNRAS, 443, 2342

Maughan, B. J., Giles, P. A., Randall, S. W., Jones, C., & Forman, W. R. 2012, MNRAS, 421, 1583
Merloni, A., Predehl, P., Becker, W., et al. 2012, arXiv:1209.3114
Migkas, K., Schellenberger, G., Reiprich, T., et al. 2020, A&A, in press
Motl, P. M., Hallman, E. J., Burns, J. O., & Norman, M. L. 2005, ApJL, 623, L63
Nagai, D., Vikhlinin, A., & Kravtsov, A. V. 2007, ApJ, 655, 98
Navarro, J. F., Frenk, C. S., & White, S. D. M. 1997, ApJ, 490, 493
Okabe, N., Zhang, Y.-Y., Finoguenov, A., et al. 2010, ApJ, 721, 875
Pacaud, F., Pierre, M., Refregier, A., et al. 2006, MNRAS, 372, 578
Pierre, M., Pacaud, F., Adami, C., et al. 2016, A&A, 592, A1
Piffaretti, R., Jetzer, P., & Schindler, S. 2003, A&A, 398, 41
Planck Collaboration, Ade, P. A. R., Aghanim, N., et al. 2011, A&A, 536, A8
Planck Collaboration, Ade, P. A. R., Aghanim, N., et al. 2014, A&A, 571, A29
Pratt, G. W., Arnaud, M., Biviano, A., et al. 2019, SSRv, 215, 25
Pratt, G. W., Croston, J. H., Arnaud, M., & Böhringer, H. 2009, A&A, 498, 361
Reichert, A., Böhringer, H., Fassbender, R., & Mühlegger, M. 2011, A&A, 535, A4
Reiprich, T. H. 2017, AN, 338, 349
Rossetti, M., Gastaldello, F., Eckert, D., et al. 2017, MNRAS, 468, 1917
Rossetti, M., Gastaldello, F., Ferioli, G., et al. 2016, MNRAS, 457, 4515
Schellenberger, G., & Reiprich, T. H. 2017, MNRAS, 469, 3738
Schellenberger, G., Reiprich, T. H., Lovisari, L., Nevalainen, J., & David, L. 2015, A&A, 575, A30
Sereno, M. 2016, MNRAS, 455, 2149
Sereno, M., & Ettori, S. 2015a, MNRAS, 450, 3633
Sereno, M., & Ettori, S. 2015b, MNRAS, 450, 3675
Sereno, M., Ettori, S., Eckert, D., et al. 2019a, A&A, 632, A54
Sereno, M., Ettori, S., Eckert, D., et al. 2019b, arXiv:1906.10455
Sereno, M., Umetsu, K., Ettori, S., et al. 2020, MNRAS, 492, 4528
Sun, M., Voit, G. M., Donahue, M., et al. 2009, ApJ, 693, 1142
Truong, N., Rasia, E., Mazzotta, P., et al. 2018, MNRAS, 474, 4089
Vazza, F., Eckert, D., Simionescu, A., Brüggen, M., & Ettori, S. 2013, MNRAS, 429, 799
Vikhlinin, A. 2006, ApJ, 640, 710
Vikhlinin, A., Burenin, R. A., Ebeling, H., et al. 2009, ApJ, 692, 1033
Vikhlinin, A., Kravtsov, A., Forman, W., et al. 2006, ApJ, 640, 691
Willingale, R., Starling, R. L. C., Beardmore, A. P., Tanvir, N. R., & O'Brien, P. T. 2013, MNRAS, 431, 394
Zhang, Y.-Y., Reiprich, T. H., Finoguenov, A., Hudson, D. S., & Sarazin, C. L. 2009, ApJ, 699, 1178
Zhuravleva, I., Churazov, E., Kravtsov, A., et al. 2013, MNRAS, 428 3274